Dependency of simulated tropical Atlantic current variability on the wind forcing

Kristin Burmeister[1], Franziska U. Schwarzkopf[2], Willi Rath[2], Arne Biastoch[2,3], Peter Brandt[2,3], Joke F. Lübbecke[2], and Mark Inall[1,4]

[1]SAMS Scottish Association for Marine Science, Oban, United Kingdom
[2]GEOMAR Helmholtz Centre for Ocean Research Kiel, Kiel, Germany
[3]Christian-Albrechts-Universitaet, Kiel, Germany
[4]University of the Highlands and Islands, United Kingdom

Correspondence: Kristin Burmeister (kristin.burmeister@sams.ac.uk)

Abstract. The upper wind-driven circulation in the tropical Atlantic Ocean plays a key role in the basin wide distribution of water mass properties and affects the transport of heat, freshwater, and biogeochemical tracers such as oxygen or nutrients. It is crucial to improve our understanding of its long-term variability which largely relies on model simulations due to sparse observational data coverage especially before the mid-2000s. We applied two different forcing products to a high-resolution ocean model which resolves the complex zonal current field in the tropical Atlantic. Where possible, we compared the simulated results to long-term observations. We found that in simulations the strength of the wind stress curl above the upwelling regions of the eastern tropical North Atlantic is important to set the mean strength of the off-equatorial surface and subsurface currents north of the equator. Too strong wind stress curl above the upwelling regions seems to overestimate the subsurface currents resulting in unrealistic seasonal variability. The simulated decadal to multidecadal variability of the tropical Atlantic current field can, to a large extent, be explained by changes in the Sverdrup dynamics. The combination of both simulations and observations reveals that the recent strengthening of the EUC can be indeed interpreted as a recovery from a weak phase the current experienced since the late 1990s. Where it has become common place for models to explain processes behind ocean observations, we postulate that long-term observations, once they have reached a critical length, can be used to test the quality of wind-driven simulations. This study presents one step in this direction.

1 Introduction

The tropical Atlantic circulation plays a crucial role in the climate relevant, basin-wide distribution of heat, freshwater, carbon and ecosystems relevant quantities in the Atlantic Ocean. A unique feature of the Atlantic Ocean is the Atlantic Meridional Overturning Circulation (AMOC). The return flow of the AMOC in the upper ocean transports heat, freshwater and biogeochemical properties like carbon or oxygen northward through the basin impacting climate and ecosystems in the entire Atlantic sector. On their way through the tropics water masses experience an important transformation gaining heat (0.22 PW, Hazeleger and Drijfhout, 2006) and salinity (freshwater divergence of 0.16Sv, Hazeleger and Drijfhout, 2006). About one third of the northward flow is recirculated within the tropical Atlantic current system (Hazeleger and Drijfhout, 2006; Tuchen et al.,

2022a). While observations allow now to describe the mean to sub-decadal variability of the upper tropical Atlantic circulation (e.g. Tuchen et al., 2022a; Brandt et al., 2021; Burmeister et al., 2020), the study of multidecadal changes and trends largely

25 rely on model output (e.g. Burmeister et al., 2019; Hüttl-Kabus and Böning, 2008; Duteil et al., 2014).

The flow field in the tropical Atlantic is part of the wind-driven gyre circulation, a superposition of shallow overturning cells, and the basin-wide AMOC (e.g. Schott et al., 2004; Hazeleger and Drijfhout, 2006; Perez et al., 2014; Tuchen et al., 2022a; Heukamp et al., 2022). In the upper ∼300 m, the shallow subtropical cells (STCs) consist of poleward Ekman transport at the surface and equatorward transport in the thermocline that connect the subduction regimes in the subtropics and the

30 upwelling regimes in the tropics (Schott et al., 2004). The tropical overturning cells (TCs) are part of the STCs and dominate the meridional flow field in the upper 100 m between 5°N and 5°S (e.g. McCreary and Lu, 1994; Schott et al., 2004; Molinari et al., 2003; Perez et al., 2014). They are governed by wind-driven equatorial upwelling, poleward Ekman transport in the upper limb, off-equatorial down-welling at about $\pm 3 - 5°$ latitude and a geostrophic flow directed equatorward in the lower limb. The shallowest overturning cell is the Equatorial Roll in the upper 80 m along the equator. The southerly wind stress across

35 the equator drives its northward flow near the surface and southward flow below (Heukamp et al., 2022). A complex system of alternating eastward and westward narrow current bands and strong western boundary currents with northward flow participate in the STCs, TCs and the Equatorial Roll (e.g. Schott et al., 2004).

To a large extent, the wind-driven gyre circulation in the tropical Atlantic can be explained by Sverdrup dynamics that is the relationship between wind stress and depth integrated meridional transport. The trade winds converge in the Intertropical Con-

40 vergence Zone (ITCZ) slightly north of the equator. The weakening of the north- and south-easterly trade winds is associated with a positive and negative wind stress curl north and south of the ITCZ, respectively. According to the Sverdrup dynamics this results in two wind-driven gyres, the tropical gyre north and the equatorial gyre south of the ITCZ (e.g., Fratantoni et al., 2000). As a consequence of the Ekman divergence south of the ITCZ, an eastward flowing geostrophic current exists between 3° and 13°N, the North Equatorial Counter Current (Fig. 1; Urbano et al., 2006). In the north and in the south, it is flanked by

45 the westward flowing North Equatorial Current (NEC) and South Equatorial Current (SEC), respectively. Associated with the northward displacement of the ITCZ, the SEC crosses the equator and literature often distinguish between a southern branch (sSEC; south of 10°S), a central branch (cSEC; south of the equator) and a northern branch (nSEC; centred at about 2°N) (e.g. Peterson and Stramma, 1991; Schott et al., 2004).

As a consequence of the thermocline sloping upward to the east, the subsurface Equatorial Undercurrent (EUC) is flowing

50 eastward in the subsurface along the equator supplying water masses from the western basin of southern subtropical origin towards the central and eastern upwelling regions (e.g. Bourlès et al., 2002; Schott et al., 2004; Brandt et al., 2006). Two off-equatorial eastward flowing subsurface currents exists in the Atlantic, the North Equatorial Undercurrent (NEUC) and the South Equatorial Undercurrent (SEUC) centred at about 5°N/S, respectively. Potential driving mechanisms of the NEUC and SEUC are still not fully understood. Assene et al. (2020) investigated the formation and maintenance of the off-equatorial subsurface

55 currents in the Gulf of Guinea and highlighted the link between submesoscale processes, mesocale vortices and mean currents which can include any of the driving mechanisms suggested in previous studies: eddy fluxes (Jochum and Malanotte-Rizzoli, 2004), meridional advection (Wang, 2005; Johnson and Moore, 1997; Marin et al., 2000; Hua et al., 2003; Marin et al., 2003;

Ishida et al., 2005), lateral diffusion of vorticity (McPhaden, 1984) and the pull by upwelling in the eastern basin (McCreary et al., 2002; Furue et al., 2007, 2009).

60   The zonal currents in the tropical Atlantic (Fig. 1) form an interhemispheric buffer for the AMOC. A quantification of the different AMOC pathways in the tropical Atlantic was done by Tuchen et al. (2022a). The main part of the upper AMOC limb enters the tropical Atlantic within the westward flowing sSEC that bifurcates into the northward flowing NBUC and the southward flowing Brazil Current at about 15°S. Within the NBC the AMOC finally crosses the equator (e.g. Schott et al., 2004; Hazeleger and Drijfhout, 2006). After overshooting the equator, the NBC partly retroflects into the zonal current field,
65   partly breaks up into northward propagating Brazil current rings (Johns et al., 2003). The EUC, NEUC and NECC feed on the retroflection of the NBC (Bourlès et al., 1999; Hüttl-Kabus and Böning, 2008; Rosell-Fieschi et al., 2015; Stramma et al., 2005). Furthermore, the NEUC and NECC are partly supplied by water masses of northern hemisphere origin from the retroflection of the NEC (e.g. Schott et al., 1998; Bourlès et al., 1999; Urbano et al., 2008). The eastward currents connect the subducted water masses from the subtropical gyres with the central and eastern upwelling regions in the tropical Atlantic thereby ventilating the
70   oxygen poor eastern basin (Stramma et al., 2008; Urbano et al., 2008; Hahn et al., 2014; Brandt et al., 2015; Hahn et al., 2017; Burmeister et al., 2019, 2020).

In the equatorial Atlantic, the semi-annual to interannual variability of the zonal flow is attributed to resonance periods of the gravest basin mode (Thierry et al., 2004; Ascani et al., 2006; d'Orgeville et al., 2007; Ding et al., 2009; Greatbatch et al., 2012; Claus et al., 2016; Brandt et al., 2016). Resonant equatorial basin modes are low-frequency standing equatorial modes
75   consisting of long equatorial Kelvin and Rossby waves (Cane and Moore, 1981). Depending on the gravity wave speed and the basin geometry, each baroclinic mode has a characteristic resonance period. The semiannual and annual zonal flow variability in the equatorial Atlantic is attributed to the resonance period of the gravest basin mode for the second and the fourth baroclinic mode, respectively (Brandt et al., 2016).

A realistic simulation of the narrow zonal current bands and their variability in the tropical Atlantic is still challenging.
80   While climate models are generally too coarse to fully resolve the tropical Atlantic current system, recent high-resolution ocean general circulation models better represent the mean state of the zonal currents (Duteil et al., 2014). Still, distinct discrepancies to ocean observation exists (Burmeister et al., 2020, 2019). Burmeister et al. (2020) showed a relationship between the zonal currents and wind stress curl variability suggesting that it is important to resolve fine wind stress curl patterns to simulate the narrow-banded zonal current system in the tropical Atlantic.

85   In this study we investigate how two different wind forcing products of different spatial and temporal resolution impact the mean state and variability of the narrow-banded zonal current system in the tropical Atlantic. The forcing products are the well established but discontinued Coordinated Ocean-Ice Reference Experiments (CORE) v2 (Griffies et al., 2009) and its successor, the JRA55-do surface dataset (Tsujino et al., 2018). The usage of the two different forcing products to drive a global ocean model covering the tropical Atlantic Ocean at eddying resolution, INALT20, provides us with two simulations which
90   both are able to resolve the complex zonal current system in the tropical Atlantic. Furthermore, we have access to over ten years of velocity observations which period is now covered by the JRA55-do forcing. This allows us to bridge the time gap between the CORE simulation and observations.

2 Data and Methods

We compare two simulations with a high-resolution global ocean circulation model forced by two different atmospheric prod-
ucts, the Coordinated Ocean-Ice Reference Experiments (CORE) v2 dataset (Griffies et al., 2009) and the JRA55-do surface
dataset v1.4.1 (Tsujino et al., 2018). We calculate current transports for the eastward flowing EUC, NEUC, SEUC and NECC
and the westward flowing nSEC utilizing an algorithm which is following the current cores (Hsin and Qiu, 2012; Burmeister
et al., 2019). The model results are compared to shipboard hydrographic and velocity observation along 23°W (e.g. Brandt
et al., 2015; Hahn et al., 2017; Burmeister et al., 2020) and 35°W (Hormann and Brandt, 2007; Tuchen et al., 2022a) as well as
current transport time series derived from moored observations at 1.2°S to 1.2°N, 23°W (Brandt et al., 2021) and 5°N, 23°W
(Burmeister et al., 2020).

2.1 High-resolution Global Ocean Circulation Model INALT20

Our analyses are based on the output of the global ocean circulation model INALT20. In INALT20 a 1/20° nest covering
the South Atlantic and the western Indian oceans between 70°W and 70°E and the northern tip of the Antarctic Peninsula
at 63°S to 10°N, is embedded into a global 1/4° host model (Schwarzkopf et al., 2019). The model is based on the Nucleus
for European Modelling of the Ocean (NEMO) v3.6 code (the NEMO team, 2016) incorporating the Louvain-La-Neuve sea-
ice model version 2 using a viscous–plastic rheology (LIM2-VP; Fichefet and Maqueda, 1997). A global configuration with
tripolar grids, named ORCA025, is used as host to build the regionally finer resolved configuration realized by the AGRIF
(Adaptive Grid Refinement in Fortran) library (Debreu et al., 2008). This set up allows for two-way interactions: the host not
only provides boundary conditions for the nest but also receives information from the nest.

The model configuration has a vertical grid with 46 z levels varying in vertical grid size from 6m at the surface to 250m
in the deepest layers, resolving the first baroclinic mode (Stewart et al., 2017; Schubert et al., 2019) which is needed for the
representation of the major baroclinic currents. The same vertical grid has proven to be an appropriate choice for simulations
with model configurations up to 1/20° horizontal resolution (e.g. Böning et al., 2016; Behrens et al., 2017). The bottom
topography is represented by partial steps (Barnier et al., 2006) with a minimum layer thickness of 25 m.

In this study we use two hindcast simulations which are forced with two different wind forcing products for the period 1958
to 2009 and 2019, respectively. Both hindcast simulations are preceded by a 30-year long spin-up integration. The spin-up
integration is initialized with temperature and salinity from the World Ocean Atlas (Levitus et al., 1998, with modifications in
the polar regions from PHC; Steele et al., 2001) and an ocean at rest. The spin-up is forced by interannually varying atmospheric
boundary conditions from 1980 to 2009 using CORE.

The well-establish but discontinued CORE forcing covers the period 1948 to 2009 (Griffies et al., 2009) and builds on
NCEP/NCAR reanalysis data merged with satellite-based radiation and precipitation, employing a set of parameter corrections
to minimize global flux imbalances. It has a horizontal resolution of 2°x2° and temporal resolution of 6-hours. CORE is limited
by the relative coarse spatial and temporal resolution and was discontinued in 2009 not covering the most recent decade of
observations. Additionally, multi-decadal variability in this data set might be problematic as it includes NCEP winds known to

exhibit spurious multidecadal wind variability (Fiorino, 2000; He et al., 2016; Hurrell and Trenberth, 1998). In the following we will refer to the model simulation forced with the CORE forcing as CORE_{sim}.

The second forcing product is the more recent JRA55-do surface dataset v1.4.1 (Tsujino et al., 2018), which we will refer to as JRA in the following. It is based on the 55-year Reanalysis project (JRA-55; e.g. Kobayashi and Iwasaki, 2016) conducted by

130 the Japan Meteorological Agency (JMA). This dataset stands out due to its higher horizontal (55 km) and temporal resolution (3 h) which now covers the entire observational period (1958 to present). Similar to CORE the surface fields from an atmospheric reanalysis are adjusted relative to reference datasets. The downwelling radiative fluxes and precipitation are based on reanalysis products in contrast to CORE, which uses satellite observations. In the following we will refer to the simulation forced with JRA as JRA_{sim}.

2.2 Shipboard observations

135

31 meridional velocity and 22 hydrographic and oxygen sections between 21°W and 28°W were obtained during cruises between 2000 to 2018 (Table A1). The velocity, hydrographic and oxygen ship sections used by this study are an extension of the data set used by Burmeister et al. (2020).

Velocity data were acquired by vessel-mounted Acoustic Doppler Current Profilers (vm-ADCPs). Vm-ADCPs continuously

140 record velocities throughout a ship section and the accuracy of 1-h averaged data is better than 2-4 cm s^{-1} (Fischer et al., 2003). Hydrographic and oxygen data obtained during CTD casts were typically taken on a uniform latitude grid with half-degree resolution. The data accuracy for a single research cruise is generally assumed to be better than 0.002°C, 0.002 and 2 µmol kg^{-1} for temperature, salinity, and dissolved oxygen, respectively (Hahn et al., 2017). The single velocity, hydrographic and oxygen ship section were mapped on a regular grid (0.05° latitude × 10 m) and were smoothed by a Gaussian filter

145 (horizontal and vertical influence (cutoff) radii: 0.05° (0.1°) latitude and 10 m (20 m), respectively). The single sections were averaged at each grid point to derive mean sections, which are again smoothed by the Gaussian filter.

To derive a second observational estimate for the mean current strength in the western basin, we additionally use 16 velocity and hydrographic ship section along 35°W from 1990 to 2006 (Table A2). This data set is used by Hormann and Brandt (2007) and Tuchen et al. (2022a). Note that shipboard velocity observations do not cover the upper most water layers. This is why

150 all ship sections are limited to the shallowest common water depth, which is 30 m. This is also the upper layer used for any transport estimation of surface currents derived from shipboard observations.

2.3 Path following transport estimation

Transports of the zonal currents in the tropical Atlantic are estimated using the model output and shipboard observations following the approach of Hsin and Qiu (2012). First the central position Y_{CM} of the current is estimated using the concept of

155 centre of mass:

$$Y_{CM}(t) = \frac{\int_{Z_l}^{Z_u} \int_{Y_S}^{Y_N} y\, u(y,z,t)\, dy\, dz}{\int_{Z_l}^{Z_u} \int_{Y_S}^{Y_N} u(y,z,t)\, dy\, dz}, \tag{1}$$

Table 1. Boundary condition for along pathway algorithm

	EUC	NEUC	SEUC	NECC	nSECu	nSECl
Z_U	$0\,\mathrm{kg\,m^{-3}}$	$24.5\,\mathrm{kg\,m^{-3}}$	$24.5\,\mathrm{kg\,m^{-3}}$	$0\,\mathrm{kg\,m^{-3}}$	$0\,\mathrm{kg\,m^{-3}}$	$24.5\,\mathrm{kg\,m^{-3}}$
Z_{Uobs}	$30\,\mathrm{m}$	$24.5\,\mathrm{kg\,m^{-3}}$	$24.5\,\mathrm{kg\,m^{-3}}$	$30\,\mathrm{m}$	$30\,\mathrm{m}$	$24.5\,\mathrm{kg\,m^{-3}}$
Z_L	$26.8\,\mathrm{kg\,m^{-3}}$	$26.8\,\mathrm{kg\,m^{-3}}$	$27.0\,\mathrm{kg\,m^{-3}}$	$24.5\,\mathrm{kg\,m^{-3}}$	$24.5\,\mathrm{kg\,m^{-3}}$	$26.8\,\mathrm{kg\,m^{-3}}$
Y_S	$1.2°\mathrm{S}$	$3.5°\mathrm{N}$	$6°\mathrm{S}$	$4°\mathrm{N}$	$0°$	$0°$
Y_N	$1.2°\mathrm{N}$	$6.0°\mathrm{N}$	$4°\mathrm{S}$	$10°\mathrm{N}$	$5°\mathrm{N}$	$4°\mathrm{N}$
W	$2°$	$2°$	$2°$	$3.5°$	$2°$	$2°$
$Y_{CM} - W$	$3°\mathrm{S}$	$2.5°\mathrm{N}$	$6°\mathrm{S}$ (model $7°\mathrm{S}$)	$2.5°\mathrm{N}$	$0°\mathrm{S}$	$0°$
$Y_{CM} + W$	$2.5°\mathrm{N}$	$8°\mathrm{N}$	$3°\mathrm{S}$	$10°\mathrm{N}$	$6°\mathrm{N}$	$5°\mathrm{N}$

Z_u (Z_l) is upper (lower) boundary of the flow, and Y_N (Y_S) is the northern (southern) limit of the current core, W is half mean width of current, $Y_{CM} + W$ ($Y_{CM} - W$) is the northern (southern) absolute limit for the flow integration. Note, as the moored and ship board observations do not cover the upper water layer, we choose the upper boundary of the flow Z_{Uobs} to be $30\,\mathrm{m}$, the shallowest common depth of all observations.

where y is latitude, u is zonal velocity, z is depth, t is time, Z_u (Z_l) is upper (lower) boundary of the flow, and Y_N (Y_S) is the northern (southern) limit of the current core.

Now the eastward velocity is integrated within a box whose meridional range is given by $Y_{CM}(t)$ and half mean width W of the flow:

$$INT(t) = \int_{Z_l}^{Z_u} \int_{Y_{CM}-W}^{Y_{CM}+W} u(y,z,t)\, dy\, dz \tag{2}$$

The boundary conditions chosen for each current are listed in table 1.

2.4 Moored transport time series

We use long term observational transport time series estimated for the EUC by Brandt et al. (2021, 2014) and for the NEUC by Burmeister et al. (2020) to validate the model simulations. Transport time series of the EUC and NEUC were reconstructed from moored velocity observations at 0°N/23°W (May 2005-Sep 2019) and 5°N/23°W (Jul 2006-Feb 2008, Nov 2009-Jan 2018), respectively.

Horizontal velocity data were acquired using moored ADCPs. At the equator the upper water column was observed by one 300 or 150 kHz upward-looking ADCP between 100 to 230 m depth and another 75 kHz ADCP either downward-looking from just below the upper instrument or upward-looking from 600 to 650 m depth. Apart from a period between 2006 and 2008, when the upper instrument failed, the velocity measurements cover the whole depth range of the EUC. At 5°N either a downward- (Jul 2006-Feb 2008) or upward-looking (Nov 2009-Jan 2018) 75 kHz ADCP was installed. The upper measurement range of the 5°N ADCPs varies between 65 and 85 m, i.e. the full extent of the NEUC (65-270m) is not always covered. The

effect of tides was removed from the moored velocity data by a 40-h low-pass Butterworth filter and subsampled to a regular

175   12-h time interval. The short term variability of the tropical Atlantic exceeds the measurement accuracy of the different ADCPs and errors in the ADCP compass calibrations are expected to be unsystematic (Brandt et al., 2021).

The EUC transport time series is estimated by regressing variability patterns derived from shipboard observations onto the moored velocity time series at 0°/23°W (Brandt et al., 2014, 2016, 2021). Eastward velocities ($u > 0$) of the reconstructed latitude-depth-sections (30-300m depth and $1°12'$S–$1°12'$N) are integrated to obtain the EUC transport. The root mean square

180   differences for the EUC transport reconstruction using the equatorial mooring is 1.29 Sv (Brandt et al., 2014).

The NEUC transport time series is estimated from shipboard and moored velocity observations using the optimal width method (Burmeister et al., 2020). First, eastward velocities ($u > 0$) of shipboard observations are latitudinally integrated between 65 and 270m depth, 4.25°N and 5.25°N. To reconstruct the latitudinally integrated velocities ($U(z)$), an optimal latitude range for the mooring at 5°N needs to be found by regressing $U(z)$ onto the shipboard eastward velocity profile at the mooring

185   position. The moored velocities are multiplied by the optimal latitude range (0.88°) and finally depth-integrated to obtain the NEUC transport time series. The root mean square difference of the reconstructed NEUC transport is 0.52 Sv (Burmeister et al., 2020).

Note that the reconstructed transport represents the current transport integrated over a fixed box. To compare transport from model output and moored observations at 23°W, we calculate the transport for the EUC and NEUC from model output as

190   integral of eastward velocity in the respective box (EUC: 30m-300m, $1°12'$S-$1°12'$SN; NEUC: 60m-270m, 4.25°N-5.25°N).

2.5   Modal Decomposition

We decompose the velocity field of both model simulations using vertical structure functions $\hat{p}_n(z)$ obtained from a mean buoyancy frequency profile derived from observations (Brandt et al., 2016). Following the approach of Claus et al. (2016), we derive $\hat{p}_n(z)$ from a mean buoyancy frequency profile obtained from 70 shipboard CTD profiles (Table A1). To obtain the

195   mean buoyancy frequency profile we use CTD profiles with a minimum depth of 1200 m within a 1°-wide squared box centred at 23°W, 0°. Then, we bin-averaged the individual temperature and salinity profiles to a uniform 10-m vertical grid with a maximum depth of 4500 m and calculate a buoyancy frequency profile for each cast separately which were then averaged to obtain the mean buoyancy frequency profile. It is important to note that baroclinic modes are only orthogonal if the velocity data is covering the complete upper 4500m depth. Missing data as typical for shipboard or moored data reduce the orthogonality and

200   introduce uncertainties in the calculation. However, consistent results between studies provide some confidence in the chosen approach (e.g. Brandt et al., 2016; Claus et al., 2016; Kopte et al., 2018).

The gravity wave speed of the first five baroclinic modes derived from observations is shown in table 2. We also derived the vertical structure functions from mean buoyancy frequency profiles using model output from JRA$_{sim}$ and CORE$_{sim}$. For the gravity wave speed, both simulations agree well with each other and, except for the first mode, with observations.

205   To estimate the contribution of the first five modes to the annual and semi-annual cycle of the zonal velocity field in the tropical Atlantic (10°S-10°N) we use the orthogonality between functions. We fit the vertical normal baroclinic modes and temporal harmonics with reduction operations as follows.

Table 2. Gravity wave speed of first 5 baroclinic modes of the gravest basin mode using squared buoyancy frequencies within a $1°$-wide squared box centred at $23°$W, $0°$ using CTD profiles as well as model output from JRA$_{sim}$ and CORE$_{sim}$.

	mode 1	mode 2	mode 3	mode 4	mode 5
CTD	2.51	1.40	0.98	0.76	0.57
JRA	3.45	1.40	1.01	0.80	0.56
CORE	3.42	1.38	1.00	0.80	0.55

Let $\hat{p}_n(z)$ be vertical normal (baroclinic) modes with

$$\int \mathrm{d}z\, \hat{p}_n(z) \cdot \hat{p}_m(z) = \delta_{n,m} \tag{3}$$

and $h_{T,\tau}(t)$ be temporal harmonic modes with period T and phase τ which fulfil

$$\int \mathrm{d}t\, h_{T,0}(t) \cdot h_{T/2,0}(t) = 0 \tag{4}$$

$$\int \mathrm{d}t\, h_{T,0}(t) \cdot h_{T,0}(t) = 1 \tag{5}$$

Then, we could compose a signal $s(t,z)$ with different normal modes each having a separate annual and semi-annual cycle as:

$$s(t,z) = \sum_n \alpha_n^a \cdot \hat{p}_n(z) \cdot h_{365d,\tau_n^a}(t) + \sum_n \alpha_n^s \cdot \hat{p}_n(z) \cdot h_{365d/2,\tau_n^s}(t) \tag{6}$$

where α_n^a are the amplitudes of the annual cycle of the baroclinic mode n, α_n^s are the amplitudes of the semi-annual cycle of the baroclinic mode n, τ_n^a is the phase shift of the annual cycle of baroclinic mode n, and τ_n^s is the phase shift of the semi-annual cycle of baroclinic mode n.

The time-variability of the baroclinic mode n can be diagnosed using a time integral:

$$\alpha_n^a \cdot h_{365d,\tau_n^a}(t) + \alpha_n^a \cdot h_{365d/2,\tau_n^a}(t) = \int \mathrm{d}z\, b_n(z) \cdot s(t,z) \equiv s_n(t) \tag{7}$$

The phase and amplitude of $s_n(t)$ can be diagnosed by projecting on a normalized annual $\mathrm{e}^{i2\pi/365d \cdot t}$ or semi-annual $\mathrm{e}^{i4\pi/365d \cdot t}$:

$$\alpha_n^a \propto \left| \int \mathrm{d}t\, \mathrm{e}^{i2\pi/365d \cdot t} s_n(t) \right|, \qquad\qquad \alpha_n^s \propto \left| \int \mathrm{d}t\, \mathrm{e}^{i4\pi/365d \cdot t} s_n(t) \right| \tag{8}$$

$$\tau_n^a = \arg\left(\int \mathrm{d}t\, \mathrm{e}^{i2\pi/365d \cdot t} s_n(t) \right), \qquad\qquad \tau_n^s = \arg\left(\int \mathrm{d}t\, \mathrm{e}^{i4\pi/365d \cdot t} s_n(t) \right) \tag{9}$$

2.6 Sverdrup Balance

The Sverdrup balance relates the meridional volume transport in the ocean interior to the wind stress curl. It can be derived from the momentum balance between the pressure gradient, the Coriolis force and wind stress (Sverdrup, 1947). We calculate

the Sverdrup stream function as follows:

$$\Psi = -\frac{1}{\rho_0 \beta}\left(\int\limits_{x}^{x_0}\left(\hat{k}\nabla\times\tau\right)\,dx\right), \qquad \beta = \frac{\partial f}{\partial y} = \frac{2\Omega\cos(\phi)}{R_{Earth}} \qquad (10)$$

230   where $\rho_0 = 1025\text{kg m}^{-3}$ is mean water density, x_0 is west coast of Africa, x is longitude, $(\hat{k}\nabla\times\tau)$ is wind stress curl, Ω=7.271$\cdot10^{-5}$ s^{-1} is the angular velocity of the Earth rotation, R_{Earth}=6.37$\cdot10^6$m is the radius of the Earth, ϕ is latitude.

2.7   Ekman transport and subtropical cells

The wind driven STCs connect subtropical subduction regions with the tropical upwelling region (e.g., Schott et al., 2004; Tuchen et al., 2019) and can impact the strength of zonal currents in the tropical Atlantic (Rabe et al., 2008). The strength of
235   the STCs is related to the Ekman divergence which is commonly defined as the difference of Ekman transport between 10°S and 10°N (Rabe et al., 2008; Tuchen et al., 2019). Assuming the upper branch of the STCs is governed by poleward Ekman transport we calculate it as follows:

$$T_E(x,y,t) = -\frac{1}{\rho_0}\frac{\tau_x(x,y,t)}{f(y)}\Delta x \qquad (11)$$

where τ_x represents the zonal wind stress component and Δx is the zonal grid spacing in the model simulation.

240   ### 2.8   Tropical instability wave activity

Part of the NEUC and SEUC are thought to be driven by mesoscale eddies or vortices, among other tropical instability waves (TIWs, e.g. Jochum and Malanotte-Rizzoli, 2004; Assene et al., 2020). To see if a different intensity of TIWs exist between the two model simulations we calculated the TIW activity from the simulated meridional velocity field at 160m depth. We first applied a 20-50 days bandpass filter, followed by a 4°-20° bandpass filter to the 5 daily meridional velocity field (v'). In both
245   cases a 2nd order, zero-phase Butterworth bandpass filter was used. Then, we calculated the monthly standard deviation from the filtered data ($\sigma(v')$). This is a well establish methods for the analysis of TIWs (Lee et al., 2014; Olivier et al., 2020; Perez et al., 2012; Tuchen et al., 2022b). Finally we box average the monthly standard deviation of meridional velocity between 3°N and 7°N, 30°W and 10°W for the NEUC and 3°S and 7°S, 30°W and 0° for the SEUC (Fig. 7).

3   Results

250   To compare the two model simulations we will focus on quantities of or derived from the wind forcing as well as quantities of or derived from the simulated velocity field. In particular we will compare zonal wind stress, wind stress curl, zonal velocity and zonal current transport and discuss it under the aspect of among others the Sverdrup Streamfuction and meridional Ekman divergence derived from the wind forcings and resonant equatorial basin modes fitted to the simulated velocity field. We will compare the mean fields, seasonal variability and longer term variability and trends. Where possible, we will evaluate the
255   simulations with observations.

3.1 Mean fields

CORE$_{sim}$ and JRA$_{sim}$ both represent the common large scale wind stress pattern in the tropical Atlantic (Fig. 1): The south-easterly trades cross the equator, leading to negative wind stress curl south of about 2°N as well as in the eastern basin west of 20°W and south of 6°N. North of the equator mainly positive wind stress curl occurs. Between 0° and 5°N west of 20°W
260   the wind stress curl is up to three times stronger in CORE$_{sim}$ than in JRA$_{sim}$ for the period 1980 to 2009. JRA$_{sim}$ resolves much finer wind stress curl structures than CORE$_{sim}$, especially along the western and eastern boundaries. Another important feature of the wind stress curl is the minimum at about 6°N which drives the sea level slope important for the NECC. This is much more pronounced in JRA$_{sim}$ compared to CORE$_{sim}$.

As a first measure to evaluate how this might impact the wind-driven current field in the tropical Atlantic, we calculated
265   the Sverdrup stream function of the temporal averaged wind stress curl (contour lines in Fig. 1). The tropical gyre north and the equatorial gyre south of the NECC are clearly visible in both simulations. In CORE$_{sim}$ the tropical gyre reaches further equatorward, especially in the western basin, compared to JRA$_{sim}$. In JRA$_{sim}$ the mean position of the NECC lines up with the zero crossing of the Sverdrup stream function between both gyres. In CORE$_{sim}$ this is the case east of 20°W, while the NECC is displaced northward of the zero crossing west of it. In general, largest differences of the Sverdrup stream function
270   between JRA$_{sim}$ and CORE$_{sim}$ occur north of the equator (Fig. 1c).

Next, we compare the mean zonal velocity field derived from repeated ship sections along 23°W and 35°W with the simulated mean zonal velocities along these latitudes in both simulations (Fig. 2a-f). Interestingly, largest differences between the simulations occur north of the equator along 23°W within the region of the NECC, the NEUC and the nSEC. CORE$_{sim}$ tends to overestimate the strength and vertical extend of these zonal currents compared to JRA$_{sim}$ and observations. At 35°W, these
275   currents are of similar strength in both simulations and compare reasonable well to observations. The zonal incoherence of the two simulations is also visible in the current transport (Fig. 2g-l). The transports of currents north of the equator diverge east of 35°W (NECC) or 30°W (NEUC, nSECl) with CORE$_{sim}$ producing stronger currents at 23°W (Fig. 2h,j,l). At 35°W, both model simulations agree well with the observations for the NEUC and nSECl and JRA only for the EUC. At 23°W transports in both simulations tend to overestimate the current transport compared to observations apart for the SEUC which observed
280   transport is about twice as high as the simulated transports. In general, CORE$_{sim}$ simulates higher transports than JRA$_{sim}$.

The large differences in the simulated currents north of the equator along 23°W are likely driven by the wind stress curl differences to the east of that section particularly in the regions near Africa and in the Gulf of Guinea. The pull of upwelling within domes or at the eastern boundary is a mechanism suggested to drive the off-equatorial eastward subsurface jets (NEUC, SEUC; Furue et al., 2007, 2009; McCreary et al., 2002), which might be one reason for the inter-simulation discrepancies of
285   the NEUC transports. Furthermore, the negative wind stress curl anomaly east of 23°W between 3° and 5°N drive eastward Sverdrup flow at 5°N strengthening the NECC and NEUC in CORE (Fig. 1c). The anomalous Sverdrup stream function also suggests that CORE drives a strong recirculation between the nSEC and NECC/NEUC which agrees with the findings of Burmeister et al. (2019) and shows enhanced westward flow along the core position of the nSEC in CORE. South of the equator away from the western boundary, the mean wind fields and the Sverdrup stream function agree well between both
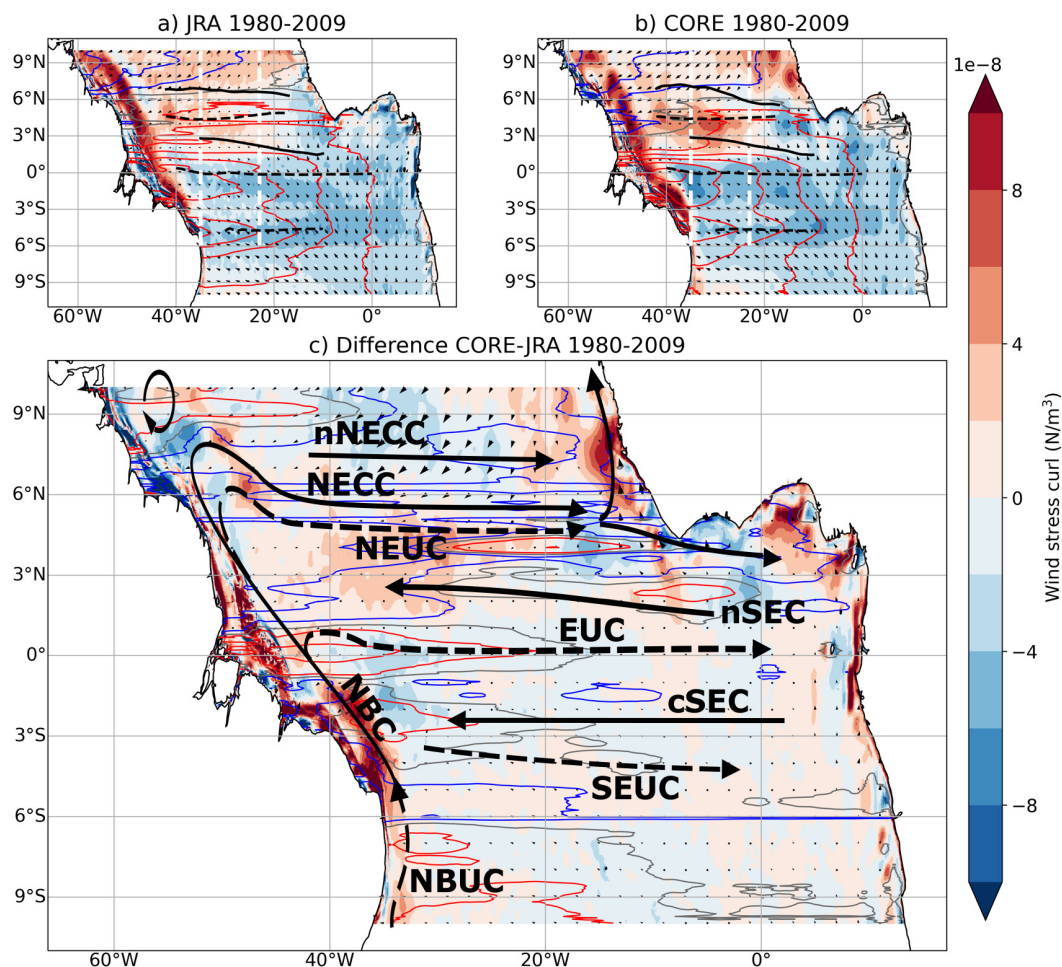
Figure 1. (a-c) 1980 to 2009 mean maps of wind stress curl (colour shading) and associated Sverdrup stream function (contour lines) calculated using (a) JRA_{sim}, (b) $CORE_{sim}$, (c) difference between both forcings. Blue contour lines show negative, red contour lines positive values of Sverdrup stream function, zero line marked as grey contour. In (a-b) the contour line interval is 2 Sv, in (c) the ± 1.5 Sv, ± 0.5 Sv isolines are shown. Zonal black lines in (a,b) mark the mean latitude (Y_{CM}, Equ. 1) of the simulated surface (solid) and subsurface (dashed) currents for the respective periods, meridional white dashed lines in (a-b) mark 35°W and 23°W sections. (c) Superimposed in black are surface (solid) and thermocline (dashed) currents (adapted from Burmeister et al., 2019, based on observations): North Equatorial Countercurrent (NECC), northern branch of the NECC (nNECC), North Equatorial Undercurrent (NEUC), northern branch of the South Equatorial Current (nSEC) and central branch of the South Equatorial Current (cSEC), Equatorial Undercurrent (EUC), South Equatorial Undercurrent (SEUC).

290 simulations while large differences exist along the western boundary. The upper SEUC is thought to be separate from the western boundary and mainly fed through recirculation with the ocean interior (Hüttl-Kabus and Böning, 2008; Fischer et al., 2008)). However, the deeper part shows a stronger connection to the western boundary with reported oxygen maxima in ship
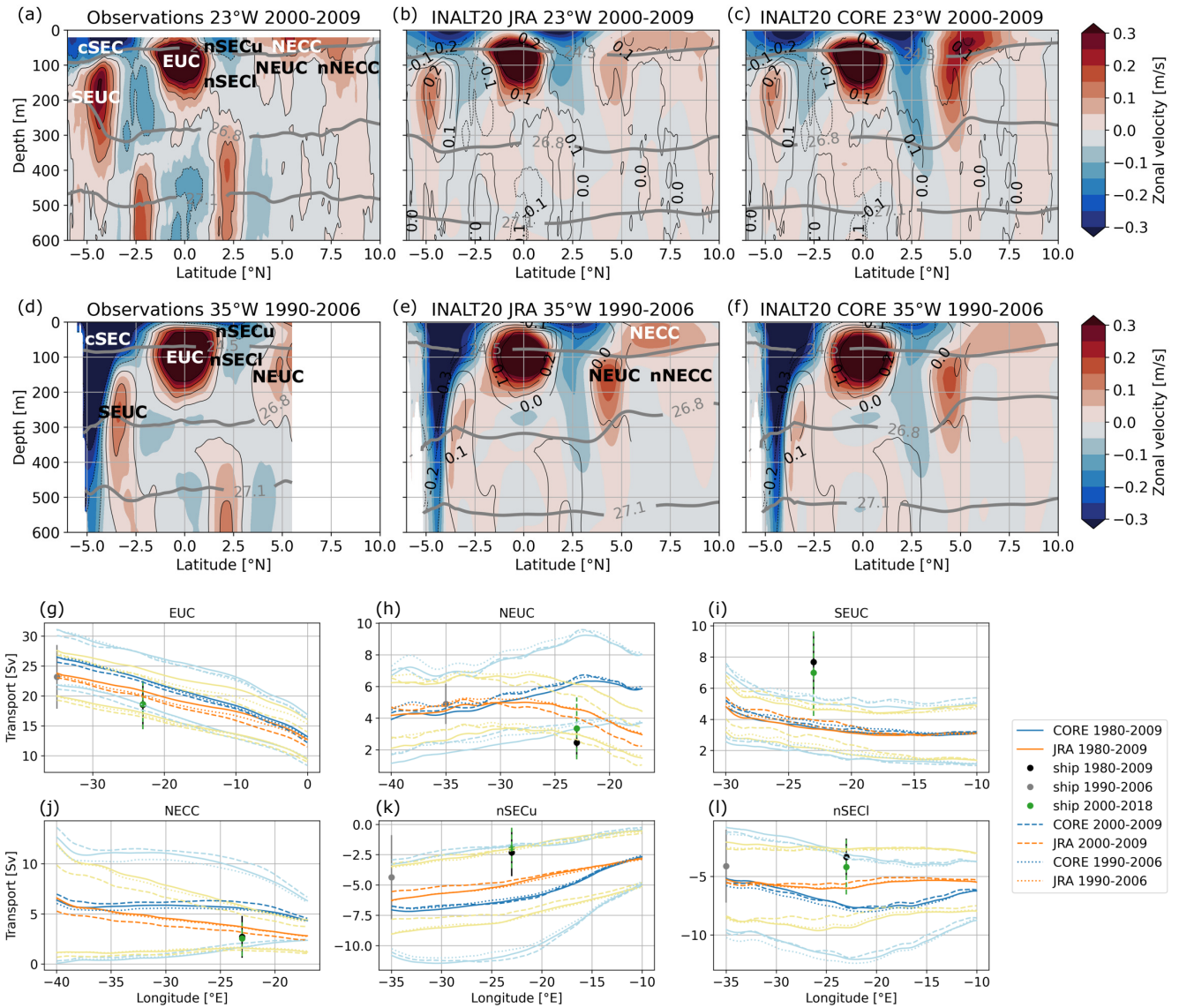
Figure 2. Mean zonal velocity along (a-c) 23°W (2000-2009) and (d-f) 35°W (1990-2006) from (a,d) observations, (b,e) JRA$_{sim}$ and (c,f) CORE$_{sim}$. Eastward velocities are positive (red), and westward are negative (blue). Grey contours mark potential density surfaces (kg/m^3). (g-l) Temporal mean transport calculated for different periods (solid: 1980-2009; dashed: 2000-2009; dotted: 1990-2006) from the CORE$_{sim}$ (blue lines) and JRA$_{sim}$ (orange lines) as well as ship sections (black dots 2000-2009, green dots 2000-2018, grey dots 1990-2006). The pastel blue and orange lines as well a the black, green and grey bars represent one standard deviation.

sections (Fischer et al., 2008). This might explain the good agreement of the mean simulated SEUC strength. However, both simulations generally underestimate the mean SEUC strength compared to observations.

295   The EUC is mainly driven by the easterly winds along the equator (Wacongne, 1989). However, Arhan et al. (2006) showed
that in the absence of the equatorial zonal wind during winter and spring, EUC transport can be remotely forced by the
wind stress curl between 2°S and 2°S connecting it to the western boundary currents. The mean wind stress (1980-2009) in
$CORE_{sim}$ along the equator is stronger (-0.034±0.012 N m^{-2}) than in JRA (-0.027±0.011 N m^{-2}). This can be one reason
why the EUC transports are stronger in CORE compared to JRA. Another process impacting the strength of the EUC is the
300   strength of the STCs. The different strength of the trade winds between the forcings may lead to a different strength in the
poleward Ekman transport forming the upper branch of the STCs which again can cause different strength in EUC (Brandt
et al., 2021). The strength of the STCs is related to the meridional Ekman divergence which is quantified as the divergence
of the Ekman transport (Equ. 11) between 10°S (JRA -9.4 Sv, CORE -11 Sv) and 10°N (JRA 9.3 Sv, CORE 11.4 Sv). The
calculated meridional Ekman divergence for both simulation (JRA 18.7 Sv, CORE 22.4 Sv) is within the range of estimates
305   derived for different wind products in Tuchen et al. (2019, 20.4±3.1 Sv). We found that the meridional Ekman divergence in
$CORE_{sim}$ is 3.7 Sv larger than in JRA_{sim}, which can contribute to a stronger mean EUC transport in $CORE_{sim}$ compared to
JRA_{sim}. Furthermore, at 35°W (23°W), the difference in the mean eastward Sverdrup transport between 2°S and 2°N for the
period 1980 to 2009 is 2.2 Sv (0.2 Sv) higher in $CORE_{sim}$ than in JRA_{sim}, which according to Arhan et al. (2006), can also
contribute to a stronger EUC in $CORE_{sim}$.

310   Summarising, CORE represents stronger trade winds, especially in the Northern hemisphere compared to JRA. This results
in stronger positive wind stress curl just north of the equator in $CORE_{sim}$. JRA resolve finer wind stress curl structures
especially along eastern basin boundary. This leads to enhanced Sverdrup transport in $CORE_{sim}$ acting to strengthen the NECC,
NEUC and nSEC especially west of 30°W. We find stronger easterly winds and higher meridional Ekman divergence between
10S° and 10°N in $CORE_{sim}$ compared to JRA_{sim} which can explain higher EUC transport. In general, mean transports of
315   simulated currents compare well to observations at 35°W, while they diverge from each other and from observations at 23°W.
Interestingly, both simulations show similar SEUC transport across the basin which is about half the magnitude of the transports
derived from ship sections along 23°W.

3.2   Seasonal cycle

The seasonal cycle in the tropical Atlantic is dominated by the meridional migration of the ITCZ and concomitant changes in
320   the wind field (e.g., Xie and Carton, 2004). In the following we will investigate how differences in the seasonal cycle of the
wind forcings impact the seasonal cycle of the zonal currents. First, we show the main patterns of the seasonal cycle of the
wind forcing by fitting the annual harmonic to the zonal wind stress and wind stress curl for the period 1980 to 2009 (Fig. 3).
Then, we describe the seasonal cycle of simulated current transports for the same period (Fig. 4). This is followed by a model
validation, where we focus on the transports of the EUC and NEUC for the period 2000-2018 when we have moored transport
325   observations available (Fig. 5). Finally, we investigate the link of the seasonal cycle between the wind forcing and the velocity
field in both simulation under the aspect of resonant equatorial basin modes (Fig. 6).

The large scale pattern of zonal wind stress and wind stress curl amplitudes of the annual harmonic cycle is similar in both
simulations while the $CORE_{sim}$ produces much higher amplitudes compared to JRA_{sim} (Fig. 3). Again, JRA resolves finer
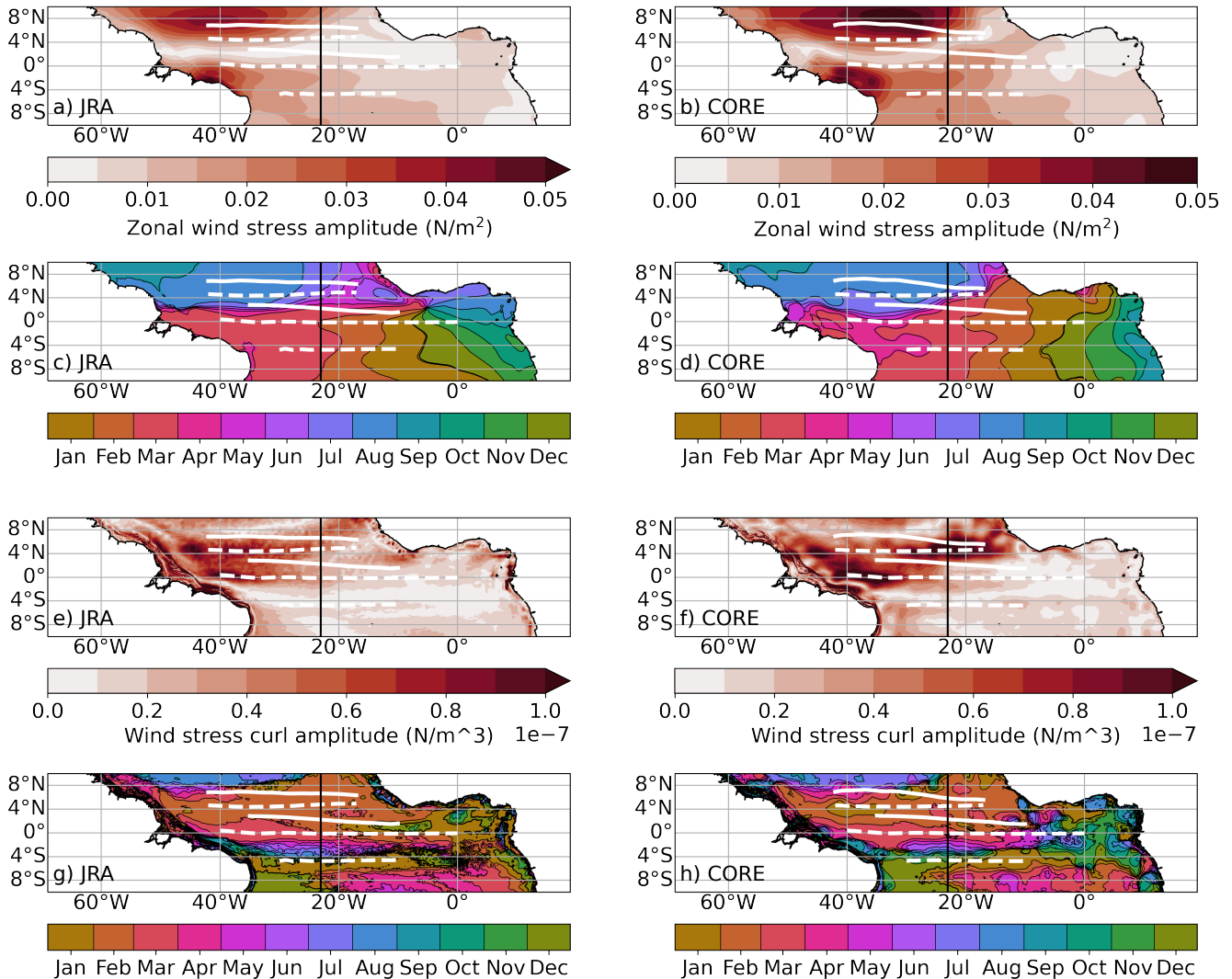
Figure 3. Amplitude (a,b,e,f) and phase (c,d,g,h) of annual harmonic fitted to monthly mean 1980-2009 climatology of zonal wind stress (a-d) and wind stress curl (e-h) from JRA$_{sim}$ (left) and CORE$_{sim}$ (right) for 1980-2009. Zonal white lines mark the mean latitude (Y_{CM}, Equ. 1) of the simulated surface (solid) and subsurface (dashed) currents for the respective periods.

wind curl structures which are not present in CORE. Largest differences occur north of the equator in the eastern basin. The
phase of the annual harmonic along the equator differs between the simulations for both, zonal wind stress and wind stress curl.
The annual harmonic amplitude of zonal wind stress along the equator is much larger in CORE compared to JRA. Before we
investigate how these differences in the wind forcing impact the zonal currents variability, we will first describe and validate
the seasonal cycle of simulated zonal current transports.

Compared to JRA$_{sim}$, CORE$_{sim}$ exhibits a stronger annual and semi-annual cycle of the zonal current transports, especially
335   at 23°W, except for the SEUC (solid lines in Fig. 4). Aligning with the results for the mean current strength, the seasonal
variability of the SEUC is very similar in both simulations and the model tends to underestimate the SEUC strength compared to
observations. At 23°W, for the EUC and nSECu, the amplitude of the annual cycle in JRA$_{sim}$ peaks in late boreal spring/early
summer, two to three months earlier than in CORE$_{sim}$. For the other currents and for the semi-annual cycle the phase in
both simulations agrees well at 23°W. Again a zonal incoherence is visible, with a general better agreement between both
340   simulations regarding the phase and amplitude of the seasonal current transports at 35°W (dashed lines in Fig. 4) than at 23°W.

To get a better understanding of how realistic the models simulate the seasonal cycle of the currents, we compare the seasonal
cycle of the simulated currents with moored transport time series available for EUC and NEUC at 23°W only. Note that the
reconstructed transports from moored observations are integrated in a fixed box. To compare transport from model output and
moored observations at 23°W, we calculated the transport for the EUC and NEUC from model output as integral of eastward
345   velocity in the respective box (EUC: 40m-300m, 1°12′S-1°12′SN; NEUC: 60m-270m, 4.25°N-5.25°N). Further more, the
transports for the seasonal, annual and semi-annual cycles in the following are calculated for a shorter time period covering the
time period of observations if possible (see caption of Fig. 5 for more detail).

At 23°W, the CORE$_{sim}$ better represents the phase of the annual cycle of the EUC (Fig. 5e-g). We found a three months
phase shift of the annual cycle in JRA$_{sim}$ compared to observations. The phase shift of the annual cycle between the CORE$_{sim}$
350   and the observations is one month (Fig. 5f). For the semi-annual harmonic JRA$_{sim}$ seems to better represent the amplitude of
the observations, while both models show a phase-shift of about one month compared to observations (Fig. 5g). Within the
chosen boundary conditions (Tab. 1), JRA$_{sim}$ cannot reproduce the EUC intensification in boreal fall which seem to be related
to the annual cycle peaking in boreal summer. Note that increasing the half mean width W in equation 2 from 2° to 3° results
in a 2 Sv increase of the seasonal cycle of EUC transport in boreal fall (2006-2018) and the fitted annual harmonic is maximum
355   at the end of July (dashed lines in Fig. 5e-g).

The representation of the NEUC transport variability is more realistic in JRA$_{sim}$ compared to the CORE$_{sim}$ (Fig. 5). JRA$_{sim}$
better captures the sporadic intra-seasonal fluctuations of the NEUC which is dominating the NEUC variability in the observa-
tions (Burmeister et al., 2020). CORE$_{sim}$ cannot reproduce these short-term fluctuations and the NEUC variability is dominated
by a strong seasonal cycle instead (amplitude of 1.8 Sv). Compared to observations, the seasonal cycle of the NEUC in JRA$_{sim}$
360   is more realistic but still too strong (JRA$_{sim}$ 0.6 Sv vs observations 0.2 Sv). JRA$_{sim}$ produces a NEUC flow maximum in
April which is not visible in the observations, but both, the simulated and observed seasonal NEUC cycle show a minimum
in boreal fall. Burmeister et al. (2020) suggested that the NEUC fluctuations might be triggered by Rossby waves which can
alter the weak eastward flow of the NEUC. They showed among others that small scale wind stress curl anomalies off the coast
of Liberia lead NEUC fluctuations by 1-2 months. Our results suggest that the JRA wind forcing seems to better resolve the
365   mechanism dominating NEUC variability, while CORE$_{sim}$ seems not to be able to resolve it. Instead, the annual cycle of the
winds stress curl in CORE$_{sim}$ shows high amplitudes within the upwelling regions of the eastern tropical North Atlantic which
might drive the seasonal cycle of the NEUC.
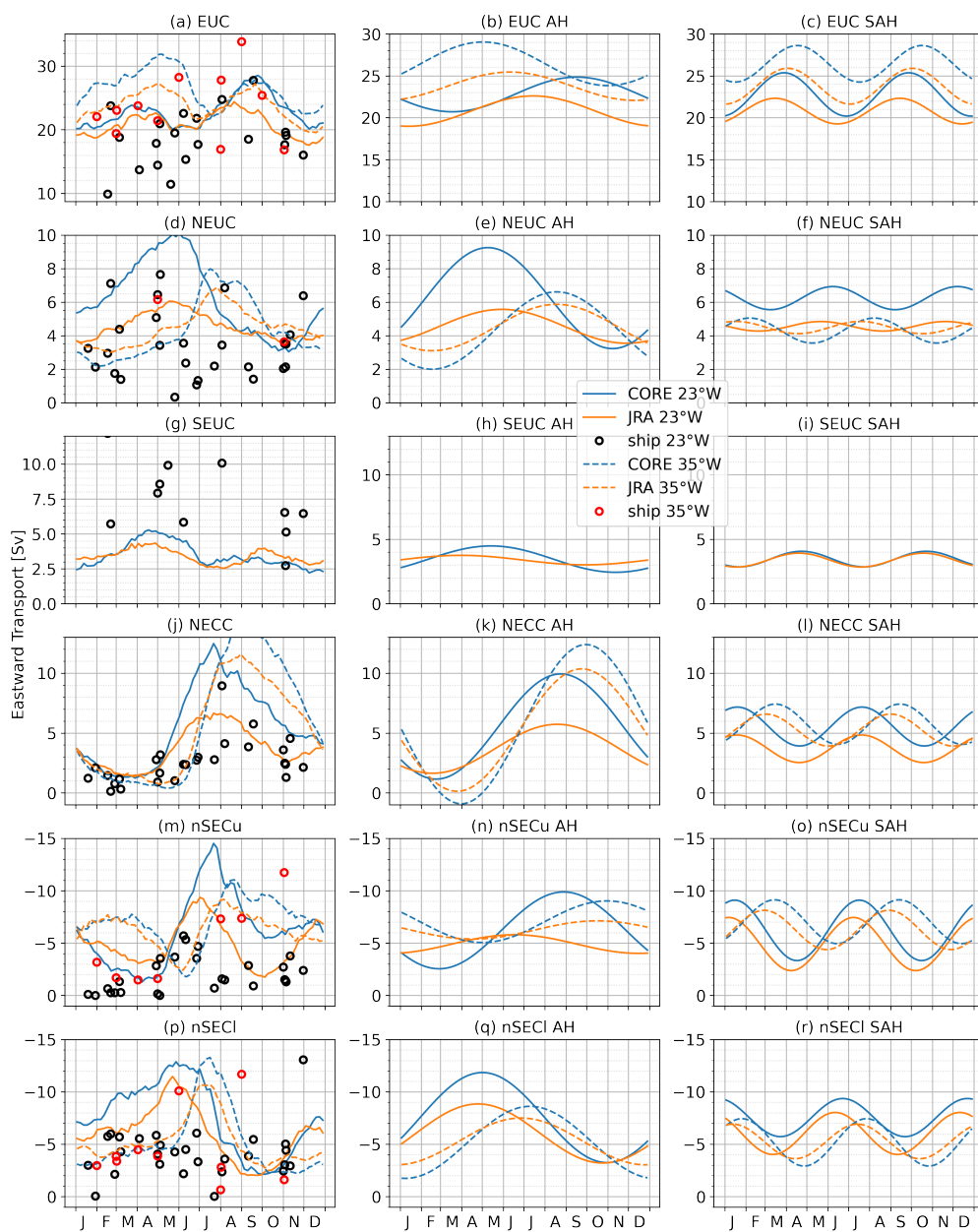
Figure 4. (left) Seasonal cycle, (middle) annual harmonic and (right) semi-annual harmonic fitted to the transport timeseries (INT, Equ. 2)) estimated from JRA_{sim} (orange lines), $CORE_{sim}$ (blue lines) at $23°W$ (solid line) and $35°W$ (dashed lines) averaged over the period 1980 to 2009. Black and red circles in the left column mark transports estimated from ship section along $23°W$ (black) and $35°W$ (red).

The semiannual and annual zonal flow variability in the equatorial Atlantic is attributed to the resonance period of the gravest basin mode for the second and the fourth baroclinic mode, respectively (Brandt et al., 2016). We performed a baroclinic modal
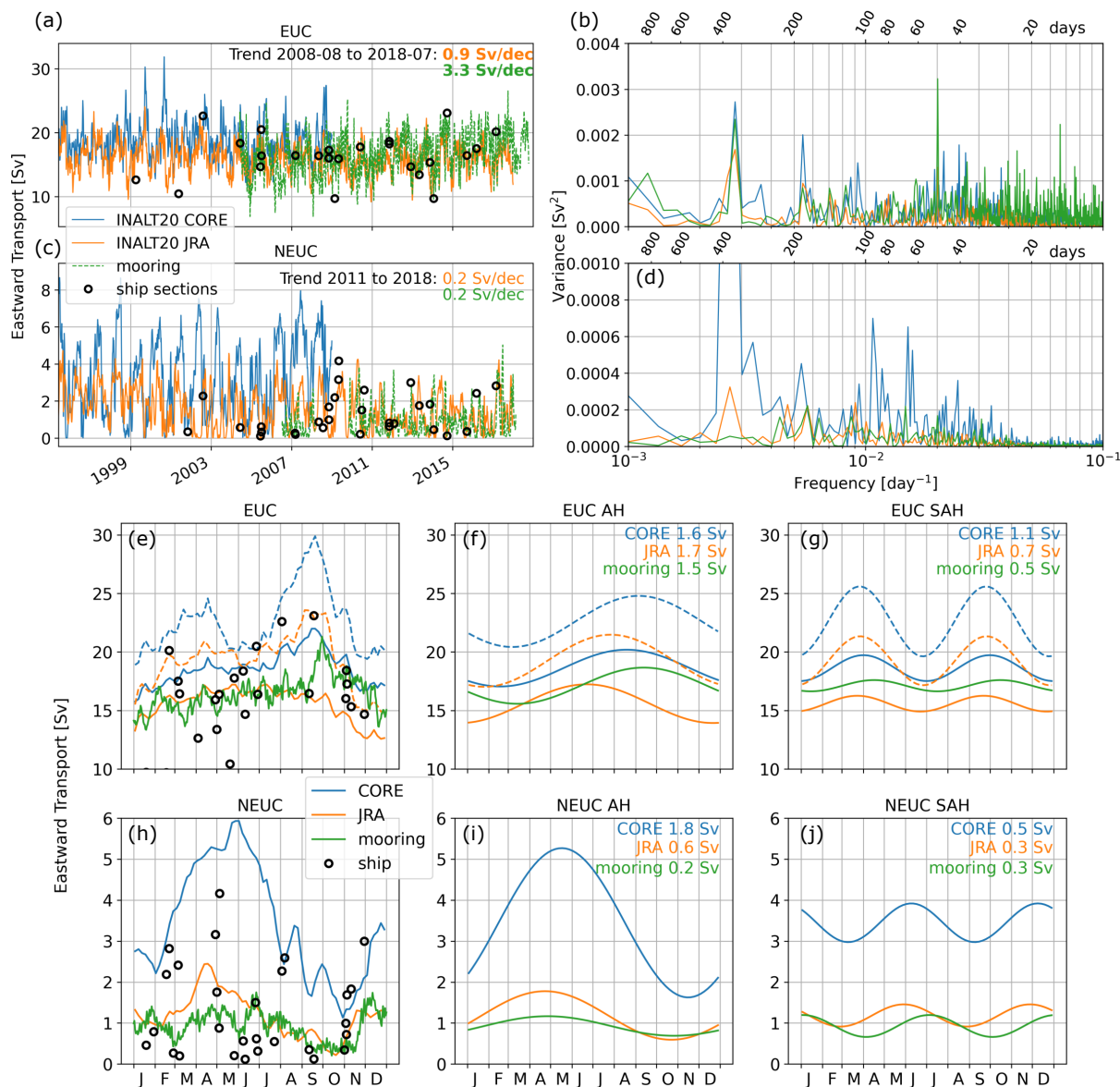
Figure 5. (a,c) Fixed box (EUC: 40m-300m, 1°12′S-1°12′SN; NEUC: 60m-270m, 4.25°N-5.25°N) eastward transport time series (solid lines) and (b,d) power spectra of the EUC (a,b) and NEUC (c,d) calculated from $CORE_{sim}$ (EUC: Jun 1996-Dec 2009, NEUC: Nov 2001-Dec 2009, blue lines), JRA_{sim} (EUC: Jun 2005-Dec 2018, NEUC: Nov 2010-Dec 2018, orange lines), moored observations (EUC: Jun 2005-Dec 2018, NEUC: Nov 2010-Dec 2018, green lines) and ship sections (black circles) at 23°W. (e,h) Seasonal cycle, (f,i) annual harmonic and (g,j) semi-annual harmonic of (e-g) EUC and (h-j) NEUC. Numbers in (f,g,i,j) represent the amplitude of the fitted harmonic cycle for each time series, respectively. The dashed lines in (e-g) show the results derived from eastward transports for the EUC calculated using Equ. 2 with a half mean width W of 3° (CORE: Jun 1996-Dec 2009, blue line, JRA: Jun 2005-Dec 2018, orange line).
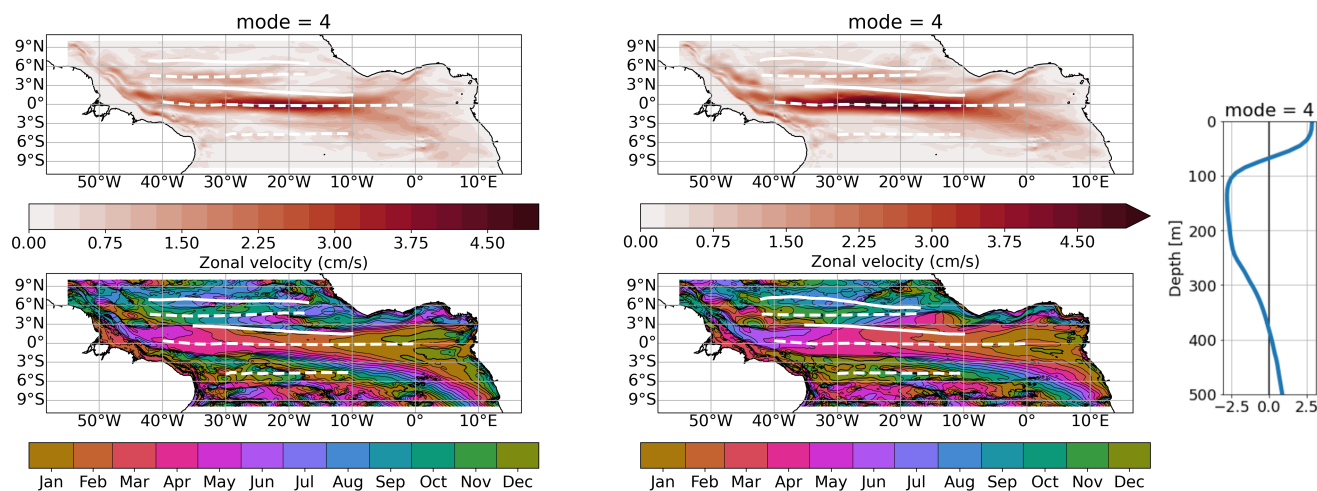
Figure 6. Amplitude (upper) and phase (lower) of fourth baroclinic mode, annual cycle of zonal velocity from JRA (left, 2000-2018) and CORE (right, 1991-2009) simulation. To derive the 3D zonal velocity field associated with the specific baroclinic mode, the amplitudes have to be multiplied by the corresponding vertical structure function shown on the right. The phase is given in month of the year when maximum eastward velocity occurs at the surface. Zonal white lines mark the mean latitude (Y_{CM}, Equ. 1) of the simulated surface (solid) and subsurface (dashed) currents for the respective periods.

370   decomposition of the zonal velocity field in both model simulations to investigate possible resonances and the dynamical response of the ocean to both wind forcings. Then, we fitted the annual and semi-annual harmonic to the first five baroclinic modes. In both simulations, we find high amplitudes of the annual harmonic along the equator for baroclinic mode four (Fig. 6) and three (Fig. A2). Along the equator, the velocity amplitudes for the seasonal cycle of barolinic mode three and four in CORE_{sim} are up to $2.5\,\mathrm{cm\,s^{-1}}$ higher than in JRA with largest difference occurring between 30°W and 20°W for baroclinic

375   mode three (Fig. A2). This is in agreement with Brandt et al. (2016) who found that the third mode in their model simulation also force with CORE was enhanced compared to observations.

Along the equator the phase of the maximum velocity of the annual cycle differs between both simulations (Fig. 6). West of 30°W along the equator, maximum velocities in the JRA_{sim} occur about one month earlier than in the CORE_{sim}. For the semi-annual cycle the differences are less distinct (Fig. A1) in agreement with the EUC transport timeseries (Fig. 5). As the

380   phase velocity of the first five baroclinic modes in both simulations are similar (Tab 2) it is likely that the differences are mainly due to the annual cycle of the wind forcing.

Along 5°N within the NEUC region, the amplitudes of the annual cycle of the fourth baroclinic mode is slightly higher in the CORE_{sim} and extends further east compared to the JRA_{sim} (Fig. 6). Largest differences in annual cycle amplitudes exists for the first two baroclinic modes just north of the NEUC mean position and south of the nSEC mean position (Fig. A2). This

385   might be one factor why we found a strong annual cycle for the NEUC in the CORE_{sim} and a weak annual cycle in the JRA_{sim}.

18

Part of the NEUC and SEUC are thought to be driven by mesoscale eddies or vortices (e.g. Jochum and Malanotte-Rizzoli, 2004; Assene et al., 2020). Among others the Eliassen-Palm flux of tropical instability waves (TIWs) are thought to maintain the eastward subsurface currents against dissipation (Jochum and Malanotte-Rizzoli, 2004). Assene et al. (2020) describe how westward propagating mesoscale vortices (e.g. TIWs) east of 20°W can created the high potential vorticity gradient in the mean fields which are associated with the NEUC and SEUC. How the mesoscale dynamics impacts the seasonal cycle of the off-equatorial subsurface current is not clear and beyond the scope of the paper. However, a difference of the seasonal cycle of the mesoscale activity between the simulations might give some indications why we found different seasonal cycles of NEUC but not for the SEUC between both models. In general, we find a higher TIW activity in $CORE_{sim}$ compared to JRA_{sim} (Fig. 7). Within the NEUC region, we found that the seasonal cycle of the TIW activity in $CORE_{sim}$ is dominated by an annual cycle and the seasonal maximum is nearly twice as high as in JRA_{sim} (Fig. 7). The seasonal cycle of the TIW activity in JRA_{sim} peaks in August and January and does not reveal a clear annual cycle. The seasonal cycle of TIW activity in the SEUC region is similar in both simulations peaking in March and August. The differences in the seasonal cycle of mesoscale activity within the NEUC region between both simulation might impact NEUC variability and hence contribute to the found transport discrepancies between both simulations.

In summary, $CORE_{sim}$ is generally forced by a stronger seasonal cycle of zonal wind stress and wind stress curl resulting in stronger current transports. Both simulations agree better in amplitude and phase of zonal wind stress and wind stress curl as well as current transport in the western basin than in the eastern basin. To investigate the dynamical response of the zonal current field to the seasonal wind forcing we performed a baroclinic modal decomposition. The phase speed of the first five baroclinic modes agree well between both simulations which suggests that the differences in the seasonal cycle of current transport are mainly attributed to differences in the wind forcings. As the subsurface off-equatorial currents are not directly wind-driven, the results are less clear for the NEUC and SEUC. Differences between the annual cycle of the first two baroclinic modes between both simulations may contribute to the discrepancies of the seasonal NEUC transports between $CORE_{sim}$ and JRA_{sim}. We also found different (similar) simulated seasonal TIW activity within the NEUC (SEUC) region between both simulations. As the NEUC and SEUC are thought to be partly eddy driven (e.g. Jochum and Malanotte-Rizzoli, 2004; Assene et al., 2020), this might be another reason for the discrepancies found in the simulated seasonal current transports. However further analysis is needed to confirm this which is beyond the scope of this paper.

3.3 Long-term variability and trends

The moored transport reconstructions give us indications for longer term changes in the zonal current field. While we cannot observe any significant trends in the NEUC transport, the EUC transport increased significantly by 3.3Sv/dec between 2008 to 2018 (Fig. 5a, Brandt et al., 2021). We also find a significant but weaker increase of EUC transport (0.9Sv/dec) in the JRA_{sim} for the same period (Fig. 5). Brandt et al. (2021) found that an intensification of trade winds in the western tropical North Atlantic and the concurrent strengthening of the STCs and enhanced Ekman divergence can explain a large part of the observed EUC intensification. In JRA_{sim} we found the Ekman divergence to significantly increase by 1.4Sv/dec between 2008 and 2018 which agrees well with the results of Brandt et al. (2021). The increase of the northeasterly trade winds might be
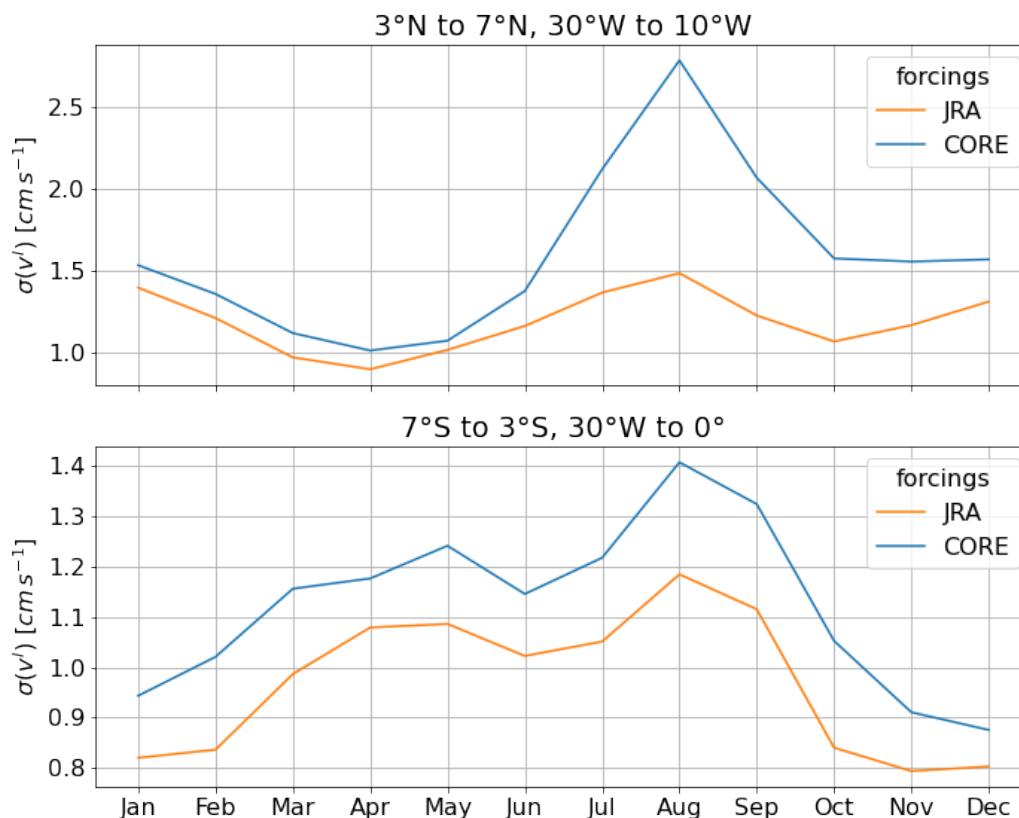
Figure 7. Monthly standard deviation of band-pass filtered meridional velocity at 160m depth from JRA_{sim} (orange line) and $CORE_{sim}$ (blue line) temporally averaged over the period 1980 to 2009 and spatially averaged within the NEUC (top) and SEUC region (bottom).

associated with the Atlantic multidecadal variability (Delworth and Greatbatch, 2000; Brandt et al., 2021), which switched from a warm phase in 2000s to a recent cold phase (Frajka-Williams et al., 2017). However, velocity observations do not extent back long enough to investigate multidecadal variability and the spread of wind trends among the available wind products is large (Brandt et al., 2021). The advantage of this study is that both model simulations go back to 1958 and which enables us to compare the multidecadal variability of the wind forcings and the simulated zonal wind-driven current field. In the following, we removed the monthly mean seasonal cycle from 1980 to 2009 and averaged the simulated timeseries annually, which reveals the interannual to multidecadal variability.

3.3.1 The wind field

The annual mean zonal wind stress anomalies in the $CORE_{sim}$ are stronger than those obtained for the JRA_{sim}, especially before 1970 (Fig. 8). While similarities between both forcings exist in the western basin, differences increase toward the east of the basin. Largest differences between both forcing products occur north of the equator before 1990.
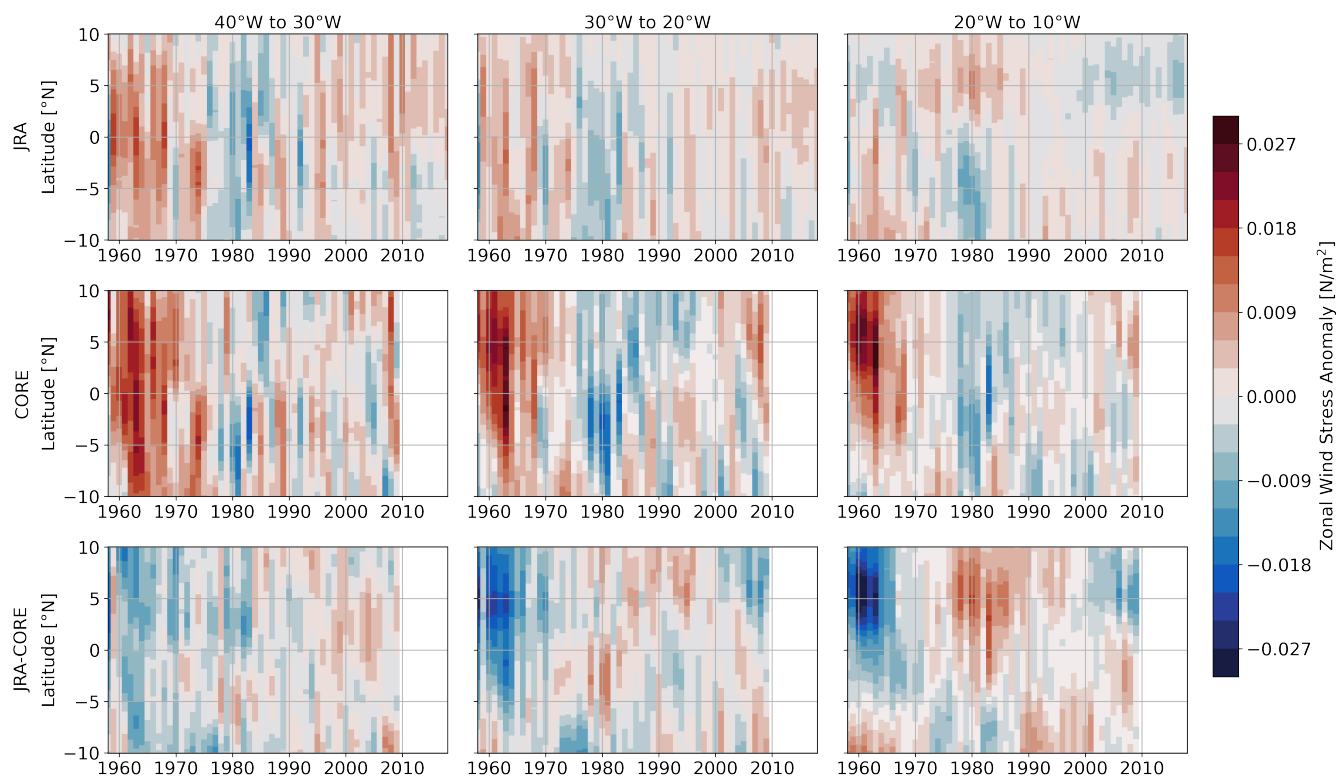
Figure 8. Hovmoeller diagram of annual mean zonal wind stress anomalies with respect to the seasonal cycle (1980-2009) zonally averaged between $40°$W and $30°$W (left), $30°$W and $20°$W (centre) and $20°$W and $10°$W (right) for JRA$_{sim}$ (upper), CORE$_{sim}$ (middle), and the difference JRA$_{sim}$-CORE$_{sim}$ (lower).

To get a first impression how these spatial dissimilarities of the wind stress anomalies impact the zonal currents, we calculated the Sverdrup stream function (Equ. 10) using the annual mean wind stress curl anomalies, which we then averaged for different time periods (Fig. 9b-f). As a reference we also calculated the Sverdrup stream function from the mean wind stress curl field from 1980 to 2009 (Fig. 9a). The spatial differences of the wind field anomalies result in distinct anomalous Sverdrup transports between the simulations, often with opposite sign for the shown periods. In the following, we will present and discuss the longer term variability and its connection to the wind field for each current separately. Therefore we calculated the annual mean anomalous volume transport for each current (Fig. 10). Additionally, we calculated the difference of the annual mean anomalous Sverdrup stream function between the approximate latitudinal boundaries (north minus south) of the currents at given longitudes (Fig. 11) assuming that the difference represents the zonal transport at that longitude (positive westward, negative eastward).

21
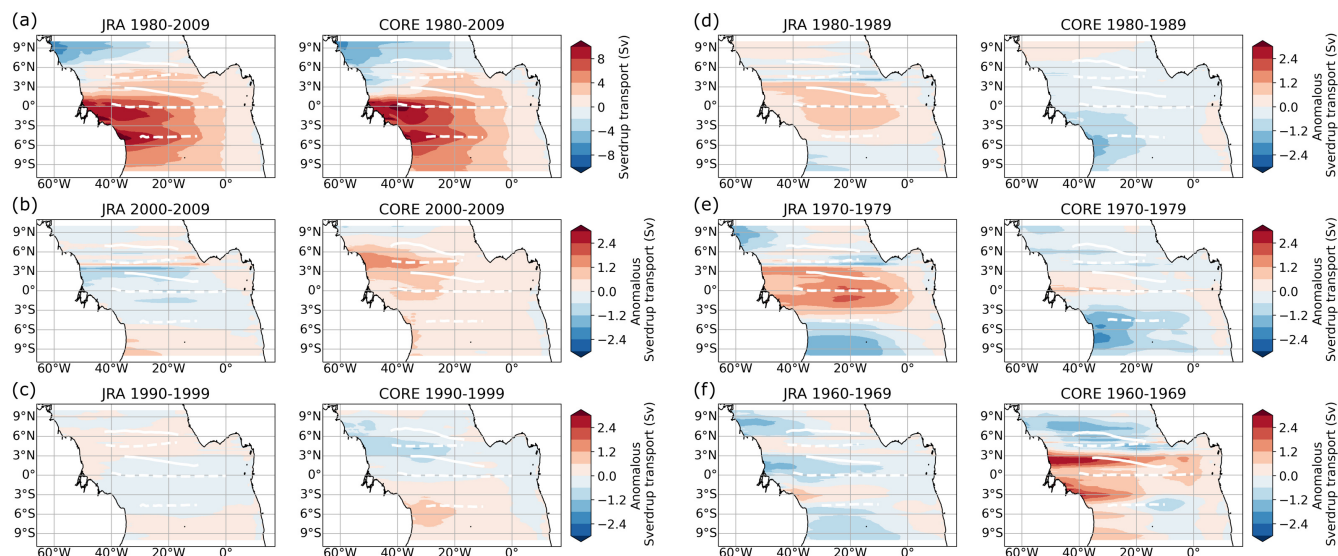
Figure 9. Sverdrup stream function calculated from (a) the 1980-2009 mean wind stress curl field, (b-g) annual mean wind stress curl anomalies averaged for the period (b) 2000-2009, (c) 1990-1999, (d) 1980-1989, (e) 1970-1979, (f) 1960-1969. In (b-f) we calculated first the Sverdrup stream function from the annual mean wind stress curl anomalies and averaged then over the respective periods. A negative stream function presents an anticlockwise rotation, this means that a zero-contour of the stream function with negative values in the south (north) marks maximum westward (eastward) velocities. Zonal white lines mark the mean latitude (Y_{CM}, Equ. 1) of the simulated surface (solid) and subsurface (dashed) currents for the respective periods.

3.3.2 EUC

Before 1980, EUC transports are generally increasing in both simulations (Fig. 10a). However, while in $CORE_{sim}$ lowest EUC transport anomalies (up to -6 Sv) across the entire timeseries occur before the mid-1970s, transport anomalies in JRA_{sim} are still slightly positive during that period. Between 1980 to 2009, the EUC decreases in both simulations (JRA -1.0 Sv/dec, CORE -0.4 Sv/dec) which is significant at a 95%-confidence level (Table 3). This is opposite to the increase of the EUC in the most recent decade (2008-2018) in observations and in JRA (Fig. 5 and Fig. 10a). Note that even though we find a strengthening of the EUC in JRA in the last 10 model years, with respect to the 1980-2009 climatology, it is still anomalous weak.

Simultaneously to the EUC strengthening before the 1980s, easterly winds along the equator are intensifying in both simulations with stronger westerly wind anomalies before 1970 in CORE compared to JRA (Fig. 8). This is accompanied by a positive trend in Ekman divergence of 3.6 Sv/dec in JRA and 3.9 Sv/dec in CORE between 1960 and 1980. Likewise, the easterlies along the equator tend to decrease after mid-1980s again and we find as well a negative trend in Ekman divergence between 1980 and 2009 of -1.5 Sv/dec in JRA and -0.9 Sv/dec in CORE. Consequently, the EUC transport weakens during this period. Still, interannual anomalies of EUC transport differ between $CORE_{sim}$ and JRA_{sim} which we link to the anomalous Sverdrup transport between 2°S and 2°N (Arhan et al., 2006). Before 1970, when westerly wind anomalies occur along the

Table 3. Linear trends per decade of transports of the currents from 1980 to 2009.

Current	Lon	JRA (sign. 95%)	CORE (sign. 95%)
		Sv/dec	Sv/dec
EUC	35°W-0°	-1.0 (True)	-0.4 (True)
NEUC	42°W-17°W	0.1 (False)	0.7 (True)
SEUC	30°W-10°W	0.4 (True)	0.3 (True)
NECC	42°W-17°W	-0.6 (True)	0.2 (True)
nSECu	35°W-10°W	0.1 (False)	0.2 (True)
nSECl	35°W-10°W	0.1 (True)	-0.2 (True)
EUC	15°W	-1.5 (True)	-0.8 (True)
NEUC	17°W	-0.6 (True)	0.2 (True)
SEUC	15°W	-0.1 (False)	0.2 (True)
NECC	17°W	-0.3 (True)	0.1 (True)
nSECu	15°W	-0.1 (False)	0.3 (False)
nSECl	15°W	0.2 (True)	0.2 (True)
EUC	25°W	-1.3 (True)	-0.3 (True)
NEUC	25°W	-0.3 (True)	0.7 (True)
SEUC	25°W	0.5 (True)	0.4 (True)
NECC	25°W	-0.5 (True)	0.3 (True)
nSECu	25°W	0.2 (True)	0.2 (False)
nSECl	25°W	0.4 (True)	-0.3 (False)
EUC	35°W	-0.7 (True)	-0.4 (True)
NEUC	35°W	0.6 (True)	0.8 (True)
SEUC	30°W	0.6 (True)	0.6 (True)
NECC	35°W	-0.8 (True)	-0.1 (False)
nSECu	35°W	0.4 (True)	0.5 (False)
nSECl	35°W	-0.5 (True)	-0.7 (False)

455 equator in both simulations, we found anomalous westward Sverdrup transports in CORE (Fig. 11) which is associated with a weakening of the EUC (Kessler et al., 2003; Arhan et al., 2006; Brandt et al., 2014). In contrast, the eastward Sverdrup transport anomalies in JRA$_{sim}$ along the equator resulting in positive EUC anomalies before mid-1970s. In the second period of anomalous weak easterlies along the equator from the early 1990s onward, the anomalous Sverdrup transport in CORE$_{sim}$ switches from eastward before 2000 to westward afterwards which impacts the EUC transports accordingly. In JRA$_{sim}$, the

460 signal in the anomalous Sverdrup transport along the equator is less clear. However, after 2010, the Ekman divergence act to

23

strengthen the EUC again while the easterly winds along the equator stay anomalous weak. The anomalous Sverdrup transport tend to be negative along the equator before mid-2010s which might counteract the EUC strengthen by the anomalous Ekman divergence.

Brandt et al. (2021) showed that the recent EUC strengthening is mainly related to trade wind changes in the western tropical North Atlantic (5°-10°N,60°-40°W) which result in the observed increased Ekman divergence in the tropical Atlantic. In agreement with Brandt et al. (2021), we find a switch from weaker northeasterly winds to stronger northeasterly winds in the western North Atlantic in the JRA_{sim} from 2010 onwards. Due to its effect on the Northern Hemisphere trade winds, Brandt et al. (2021) suggested a link between EUC transport variability and the Atlantic Multidecadal Variability (AMV). The AMV transitioned from a cold to warm phase from 1970 to 2010 and from a warm to cold phase before 1970 and after 2010. The northeasterly wind is weakest during a warm AMV phase. In general, our results support the idea that the multidecadal variability of the EUC is connected to the AMV through anomalous Ekman divergence which act to strengthen (weaken) the EUC during a cold (warm) phase of the AMV.

3.3.3 NEUC

West of 30°W, NEUC transports in both simulation decrease before 1980, and increase afterwards (Fig. 10b). At 35°W we find a significant trend of 0.6 Sv/dec in JRA_{sim} and 0.8 Sv/dec in $CORE_{sim}$ between 1980 and 2009 (Tab. 3). While this signal is zonally coherent in $CORE_{sim}$, we find significant negative trends in current transport east of ∼30°W. In the zonally averaged transports we cannot find a significant trend in JRA_{sim}, while NEUC transport are strengthening by 0.8 Sv/dec in $CORE_{sim}$.

In JRA_{sim} anomalies of zonal winds north of the equator are also not zonally coherent (Fig. 8). West of 20°W in JRA_{sim} the easterlies north of the equator are strengthening before 1980, while they are weakening after 1980. In contrast in JRA_{sim} west of 20°W the anomalies are reversed. In JRA_{sim} between 4°N and 6°N, the anomalous Sverdrup stream function drives eastward flow when the western NEUC is anomalous strong, and westward flow when the western NEUC is anomalous weak (Fig. 11). The mean NEUC position west of 30°W is located along zero-contours of the anomalous Sverdrup stream function for all decades except for the 1990s (Fig. 9). East of 30°W the position of the NEUC is displaced northward of the zero-crossings which might explain why the NEUC anomalies are not zonally coherent.

In the $CORE_{sim}$, the NEUC anomalies are generally associated with a strengthening/weakening of zonal easterly winds just north of the equator (weakening/strengthening of NEUC). Burmeister et al. (2019), who studied the NEUC in another ocean general circulation model forced by CORE (TRATL01) found the decadal to multidecadal variability of the NEUC was associated with the wind stress curl south of the equator and a resulting anomalous Sverdrup transport in the latitude range of the NEUC. In $CORE_{sim}$ we found similar wind stress curl anomalies south of the equator (10°S-0°, 35°-15°W) which are negative before the 1970s and after 1990s and positive between 1970 and 1990. However, a clear link to the anomalous Sverdrup circulation cannot be found (Fig. 9 and 11).

Tuchen et al. (2022b) recently reported multidecadal variability in TIW activity. As part of the NEUC is eddy driven (e.g. Jochum and Malanotte-Rizzoli, 2004; Assene et al., 2020), this might lead to long-term changes in the NEUC transports. However, we could not find a clear connection between long-term changes in TIW activity and NEUC transports (Fig. A3).
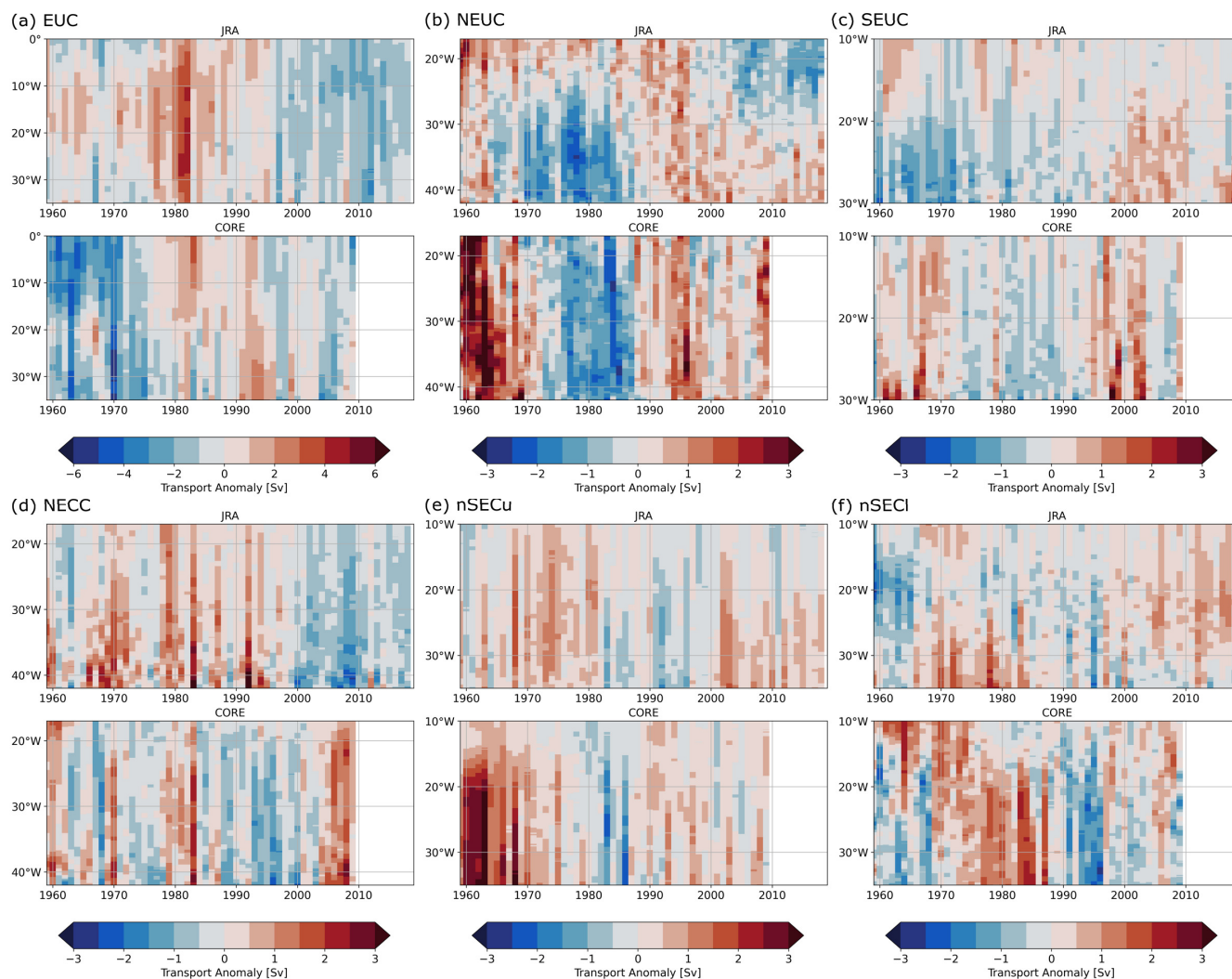
Figure 10. Hovmoeller diagram of annual mean transport anomaly (Sv) with respect to the seasonal cycle (1980-2009) for (a) EUC (eastward current), (b) NEUC (eastward current), (c) SEUC (eastward current), (d) NECC (eastward current), (e) nSECu (westward current) and (f) nSECl (westward current).

3.3.4 SEUC

Both forcings simulate a significant increase of SEUC transports (JRA 0.4 Sv/dec, CORE 0.3 Sv/dec) between 1980-2009 (Table 3). Anomalies of the long-term variability of the SEUC also tend to be zonally coherent in the CORE$_{sim}$, while they can be of opposite sign east and west of about 20°W in the JRA$_{sim}$ (Fig. 10c). In both simulations, highest anomalies occur west of 20°W. In the JRA$_{sim}$, the SEUC west of 20°W transits from a negative phase before mid-1990s to a positive phase afterwards.
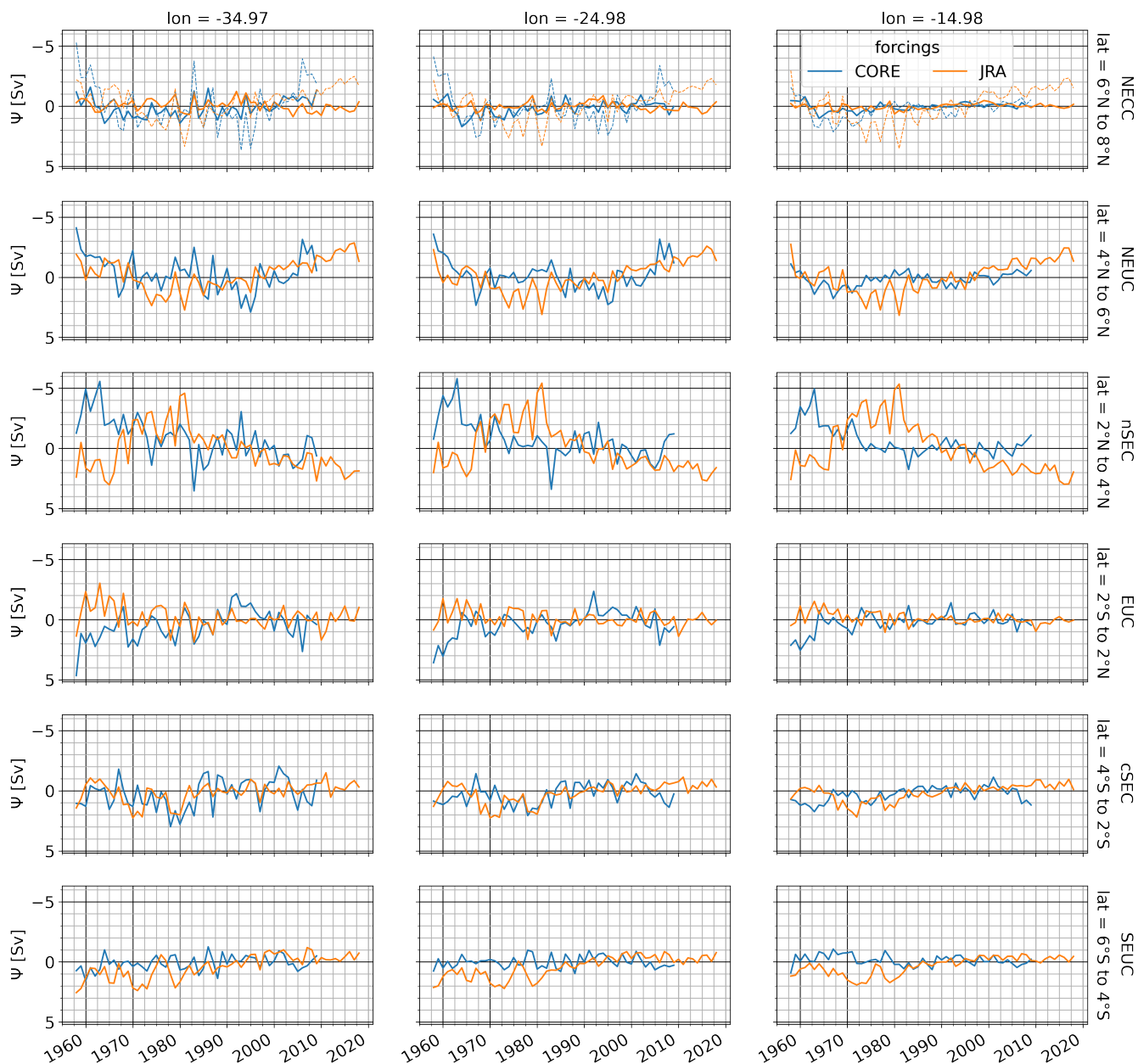
Figure 11. Difference of anomalous Sverdrup stream function Ψ with respect to 1980-2009 climatology calculated for different latitude bands centred above zonal current (rows, southern minus northern Ψ-value) for given longitudes (columns) for JRA_{sim} (orange) and CORE_{sim} (blue). Dashed lines in NECC row show the different of Ψ between 4°N and 8°N as the NECC overlaps with the NEUC core position. Note that the y-axis is reversed as negative values indicate eastward flow anomalies.

500 Likewise, the anomalous Sverdrup stream function acts to weaken (strengthen) the eastward flow of the SEUC before (after) the 1990 (Fig. 11). East of 20°W the SEUC in the JRA_{sim} varies by about 1-2 Sv on interannual to decadal timescales.

In the $CORE_{sim}$, the SEUC seems to covary with the NEUC on multidecadal timescales and we found anomalous negative (positive) wind stress curl averaged in a box south of the equator (10°S-0°, 35°-15°W) before the 1970s and after 1990s (between 1970 and 1990). The zonal flow associated with the anomalous Sverdrup stream function between 4°S and 6°S

505 shows no clear link to the SEUC transport variability on decadal to multidecadal timescales but might explain some of the interannual variability (Fig. 11). The SEUC position in CORE seems to coincide with the maximum Sverdrup stream function which indicates a meridional exchange with its flanking westward current bands of the cSEC (Fig. 9). Previous studies showed that the SEUC is mainly fed through recirculation with the ocean interior (Hüttl-Kabus and Böning, 2008; Fischer et al., 2008)) and mesoscale eddy fluxes or mesoscale vortices are suggested to be one of the drivers of the SEUC (Jochum and Malanotte-

510 Rizzoli, 2004; Assene et al., 2020). As for the NEUC, however, we could not find a clear connection between long-term changes in TIW activity and SEUC transports (Fig. A3).

3.3.5 NECC

NECC transport anomalies tend to be zonally coherent in both simulations (Fig. 10d), however after mid-1980s the anomalies are of different sign in JRA and CORE. We find a decrease of -0.6 Sv/dec of the NECC transports in JRA, and an increase

515 of 0.2 Sv/dec in CORE between 1980 to 2009 (Table 3). The NECC anomalies after 1990 are associated with an anomalous Sverdrup stream function of opposite sign in the NECC region between JRA and CORE (Fig. 9b,c and 11). In CORE, the zonal flow associated with the anomalous Sverdrup stream function between 4° and 8°N seem to better represent the long-term variability of the NECC while in JRA the anomalous Sverdrup stream function between 6° and 8°N seems to dominate flow variability.

520 Goes et al. (2013) and Hormann et al. (2012) suggest a link between the NECC variability and the Atlantic Meridional Mode, one of the dominant modes of Tropical Atlantic Variability which is acting on interannual to decadal timescales. The Atlantic Meridional Mode is characterized by a cross-equatorial sea surface temperature (SST) gradient and anomalous meridional winds blowing from the colder to the warmer hemisphere. It is mainly governed by the wind-evaporation-SST feedback Carton et al. (1996); Chang et al. (1997). Goes et al. (2013) found a positive correlation between the NECC transports and the

525 meridional wind stress anomalies averaged in the box 0°-5°N, 35°-15°W just south of the NECC. We find a similar relationship on interannual to decadal timescales in both simulation (Fig. A4), despite the distinct inter-simulation discrepancies of the NECC on multidecadal timescales.

3.3.6 nSEC (upper and lower)

The variability of the westward nSEC at the surface is dominated by a strong weakening (positive transport anomaly in Fig.

530 10e) in the $CORE_{sim}$ before the 1970 associated with a weakening of the trade winds (positive anomaly in Fig. 8d-e). In the JRA_{sim} , the nSEC at the surface tends to be stronger in the first 5 years of the simulation evolving into a weaker phase in the early 1960, getting stronger again in the early 1980s and weakens after 2000. For the lower part of the nSEC (Fig. 10f),

both simulations tend to be in a better agreement regarding the long-term variability with stronger nSEC flow before 1970 and during late-1980s to late 1990s, and weaker flow between 1970-late 1980s and after late 1990s. However, in the $CORE_{sim}$

535   anomalies are stronger and seem to propagate from the eastern to the western basin while this is less clear in the JRA_{sim}. The anomalies of the nSECu and nSECl seem to be largely in phase in the JRA_{sim}, while they tend to vary out of phase in the $CORE_{sim}$. Interestingly in the JRA forced simulation after 1980, the nSEC and the NECC are both strengthening or weakening at the same time, while this link is less clear before the 1980s in JRA forced simulation and in the CORE forced simulation. The nSEC in JRA_{sim} and the nSECu in $CORE_{sim}$ seems mainly to be associated with easterly wind anomalies just along the

540   equator (Fig. 8). The nSECl in the $CORE_{sim}$ tends to be anti-correlated with the zonal wind field.

     For the nSECu (surface), JRA_{sim} simulates no significant trend, while $CORE_{sim}$ shows a decrease of 0.2 Sv/dec between 1980 to 2009. For the same period, the nSECl (subsurface) in JRA_{sim} weakens by 0.1 Sv/dec, while transports strengthened by -0.2 Sv/dec in $CORE_{sim}$ (Table 3). This agrees with the weakening easterly winds along the equator.

4   Summary

545   In this study we investigate the effect of different wind forcings onto the representation of zonal current strength and variability in the tropical Atlantic in a general ocean circulation model. The first forcing product is the CORE v2 dataset covering the period 1948 to 2009 (Griffies et al., 2009). It has a horizontal resolution of $2° x 2°$ and temporal resolution of 6-hours. The second forcing product is the JRA55-do (JRA) surface dataset (Tsujino et al., 2018). This dataset stands out due to its high horizontal (55 km) and temporal resolution (3 h) which covers the entire observational period (1958 to present). Where

550   possible, we compared the results to ship sections and moored transport reconstructions along $23°W$ and $35°W$ (Brandt et al., 2021; Burmeister et al., 2020; Tuchen et al., 2022a). We used zonal wind stress, wind stress curl and Sverdrup anomalies to investigate the effect of the wind forcings on the zonal flow field.

     The wind stress field of the CORE forcing is generally stronger than that of the JRA forcing on all timescale (Fig. 2, 3, 8, 9). In the mean fields between 1980 and 2009, JRA_{sim} seems to better represent the EUC, NEUC, NECC and nSECl while

555   both simulations underestimate the mean transport of the SEUC compared to observations (Fig. 2). In the western basin along $35°W$, the mean simulated current transports agree well. We found stronger positive wind stress curl in CORE at the western boundary as well as north of the equator in the central basin along $5°N$, above the Guinea Dome region and along the coast of Northwest Africa (Fig. 1). South of the equator away from the western boundary the mean wind stress curl fields agree well. The large differences in the simulated currents north of the equator along $23°W$ are likely driven by the wind stress curl

560   differences in the eastern tropical North Atlantic.

     One of the reasons for the inter-simulation discrepancies might be the coarser spatial resolution of the CORE forcing. Due to its high spatial resolution, the JRA forcing is thought to better resolve fine wind stress curl structures. To get an idea how much the spatial resolution matters, we bin-average the wind stress fields of both simulation to a spatial resolution of $2°×2°$ (Fig. A5). $CORE_{sim}$ still shows increased positive wind stress curl along the wester boundary, in the central basin along $5°N$, within

565   Guinea Dome region and along Northwest Africa compared to JRA_{sim}. However, in the coarser resolution fields small features

of the Sverdrup stream function do not show up any more. In original resolution of the simulations these small scale features act to enhance mean nSEC and NECC/NEUC in $CORE_{sim}$ (Fig.1). This suggests that the resolution of the wind forcing can explain some part of the difference between the simulation, but not all of it.

$CORE_{sim}$ generally is forced by a stronger seasonal cycle of zonal wind stress and wind stress curl resulting in a stronger
570 seasonal cycle of current transport compared to JRA_{sim}. Similar to the mean fields, both simulations agree better in amplitude and phase in the western basin than in the eastern basin. Higher wind stress curl amplitudes of the annual cycle in $CORE_{sim}$ above the upwelling region of the eastern tropical North Atlantic might be one factor for the inter-simulation discrepancies in current transports north of the equator (Fig. 3). To further asses the dynamical response of the zonal current field to the seasonal wind forcing we performed a baroclinic modal decomposition (Fig. 6). The phase speed of the first five baroclinic modes agree
575 well between both simulations (Tab. 2) which indicates that the differences in the seasonal cycle of current transport are mainly attributed to differences in the wind forcings. As the subsurface off-equatorial currents are not directly wind-driven, the results are less clear for the NEUC and SEUC. Differences between the annual cycle of the first two baroclinic modes between both simulations may contribute to the discrepancies of the seasonal NEUC transports between $CORE_{sim}$ and JRA_{sim}. The NEUC and SEUC are thought to be partly eddy driven (e.g. Jochum and Malanotte-Rizzoli, 2004; Assene et al., 2020). We found
580 different (similar) simulated seasonal TIW activity within the NEUC (SEUC) region between both simulations. This might contribute to the found discrepancies and similarities of the simulated seasonal NEUC and SEUC transports, respectively. However further analysis is needed to confirm the connection between TIW strength and current transports which is beyond the scope of this paper.

For the interannual to longer term variability we found some similarities for the current strength of the NEUC and nSECl
585 between both simulations (Fig. 10b,f) while there is low agreement for EUC, SEUC, NECC, nSECu (Fig. 10a,c,d,e). East of 20°W and north of the equator, JRA_{sim} and $CORE_{sim}$ show opposite sign of annual mean zonal wind stress anomalies (Fig. 8g-i). The difference of the spatial pattern of wind field anomalies results in different anomalous Sverdrup flow (Fig. 9 and 11). Most of the differences in the long-term current variability between both simulations can be attributed to the anomalous Sverdrup flow caused by the different spatial patterns of wind stress curl. Even though the NEUC and SEUC are partly eddy
590 driven, we did not find a clear link between the long-term variability of TIWs and the strength of the off-equatorial subsurface currents (Fig. A3).

5 Conclusions

The JRA forcing is the successor of the CORE forcing for several ocean general circulation models. The application of the two different forcing products to a high-resolution ocean model, INALT20, provides us with two simulations resolving the complex
595 zonal current field in the tropical Atlantic and allowed us to compare the impact of different forcings on the ocean current field. Even though forced model simulations are needed to investigate the decadal to multidecadal variability of ocean currents, it did not escape our notice that, without observations, we cannot validate which of the simulated multidecadal variability is more realistic. However, as the JRA forcing covers the modern period of observations and the period of the CORE forcing, JRA is

forming a bridge to fill this knowledge gap. For example, Brandt et al. (2021) observed a strengthening of the EUC between

600   2008 and 2018, which we also found in JRA$_{sim}$. Looking at the entire simulation period however, both simulations suggest that the EUC strength is in a weak phase since the late 1990s and it is still recovering (Fig. 10). The model results support the assumption of Brandt et al. (2021) that the multidecadal EUC variability is linked to the Atlantic Multidecadal Variability. Another example is that Goes et al. (2013) suggested a link between the NECC and meridional wind stress anomalies just south of the current, which are concomitant with the Atlantic Meridional Mode. Despite distinct inter-simulation discrepancies

605   of the NECC long-term variability, both model simulations support the link between the NECC strength the meridional wind stress south of it on interannual to decadal timescales (Fig. A4).

Where it has become common place for models to explain processes behind ocean observations, we postulate that velocity observations, once they have reached a critical mass, can be used to test the quality of wind-driven simulations. This paper presents one step in this direction. CORE and JRA are both used in many published analysis. Here we have revealed some of

610   their relative and absolute strengths and weaknesses simulating the upper wind-driven circulation in the tropical Atlantic.

Code and data availability. All necessary code for the data analysis and preparation of the figures of this manuscript is freely available at https://github.com/Kristin-2002/Wind_forcing.git. All observational data supporting the findings of this study are publicly available as referenced within the paper. Model output necessary to reproduce the presented findings are available at https://data.geomar.de/downloads/20.500.12085/77c0d676-1933-4f17-9849-5ea2161736eb/.

615   **Appendix A**

Table A1. Meridional ship sections taken between 21°W and 28°W from 2000 to 2018. For all sections ADCP data is available. Sections including hydrography (CTD) measurements are marked accordingly. This data set is a extension of the data set used by Burmeister et al. (2020).

cruise	date	averaged longitude	latitude	depth (m)	CTD
Meteor M47*	Mar-Apr 2000	23°W	5°S-4°N	500	yes
Meteor M53	May 2002	28°W	5°S-2.5°N	500	yes
Meteor M55	Oct-Nov 2002	24°W	0°-10°N	500	no
Sonne S170	May 2003	28°W	6°S-2.5°S	800	yes
Ronald H. Brown A16N	Jun-Aug 2003	26°W	6°S-10°N	400	no
Polarstern ANTXXII/5	Jun 2005	23°W	6°S-14°N	250	no
Ronald H. Brown PNE6*	Jun 2006	23°W	5°S-13.5°N	800	yes
Ronald H. Brown PNE6*	Jun-Jul 2006	23°W	5°S-14°N	800	yes
Meteor M68/2*	Jun-Jul 2006	23°W	4°S-14°N	800	yes
L'Atalante IFM-GEOMAR 4*	Feb 2008	23°W	2°S-14°N	350	yes
L'Atalante IFM-GEOMAR 4	Mar 2008	23°W	2°S-14°N	300	no
Polarstern ANTXXV/5	Apr-May 2009	23°W	6°S-14°N	250	no
Ronald H. Brown PNE09*	Jul-Aug 2009	23°W	0°-14°N	600	no
Meteor M80/1*	Oct-Nov 2009	23°W	6°S-14°N	500	yes
Polarstern ANTXXVI/1	Oct-Nov 2009	23°W	6°S-14°N	250	no
Meteor M81/1	Feb-Mar 2010	21°W	6°S-13°N	1200	no
Polarstern ANTXXVI/4	Apr-May 2010	23°W	5°S-13.5°N	250	no
Ronald H. Brown PNE10*	May 2010	23°W	0°-14°N	650	yes
Maria S. Merian MSM18/2*	May-Jun 2011	23°W	0°-14°N	600	no
Maria S. Merian MSM18/3	Jun 2011	23°W	4°N-14°N	500	yes
Ronald H. Brown PNE11	Jul-Aug 2011	23°W	0°-14°N	600	no
Maria S. Merian MSM22*	Oct-Nov 2012	23°W	6°S-8°N	600	yes
Maria S. Merian MSM22	Oct-Nov 2012	23°W	0°-14°N	600	no
Ronald H. Brown PNE13a	Jan-Feb 2013	23°W	0°-14°N	600	no
Ronald H. Brown PNE13b*	Nov-Dec 2013	23°W	6°S-14°N	700	yes
Meteor M106*	Apr-May 2014	23°W	6°S-14°N	500	yes
Polarstern PS88.2*	Oct-Nov 2014	23°W	2°S-14°N	1200	yes
Endeavor EN-550*	Jan 2015	23°W	2°S-14°N	700	yes
Meteor M119*	Sep-Oct 2015	23°W	5.5°S-14°N	600	yes
Meteor M130*	Aug-Oct 2016	23°W	6°S-14°N	600	yes
Ronald H. Brown PNE17*	Feb-Mar 2017	23°W	4°S-14°N	700	yes
Meteor M145*	Feb-Mar 2018	23°W	6°S-14°N	700	yes

*Cruises used to derived the buyoance frequency profile at 23°W, 0°

Table A2. Meridional ship sections taken at 35°W from 1990 to 2006. For all sections ADCP and hydrographic data is available. This data set is from Hormann and Brandt (2007)

cruise	date	longitude	latitude	depth (m)*
Meteor M14/2	Oct 1990	35°W	5°S-2.5°N	full
Meteor M16/3	Jun 1991	35°W	5.5°S-2.5°N	full
Meteor M22/2	Nov 1992	35°W	5°S-4°N	full
L'Atalante - CITHER 1	Feb 1993	35°W	5°S-7.5°N	600
Meteor M27/3	Mar 1994	35°W	5°S-4.5°N	full
Le Noroit - ETAMBOT 1	Sep 1995	35°W	5°S-7.5°N	200
Edwin A. Link ETAMBOT 2	Apr 1996	35°W	4.5°S-7.5°N	full
La Thalassa - Equalant 99	Aug 1999	35°W	5°S-7 °N	full
Meteor M47/1	Mar 2000	35°W	5°S-5°N	full
Sonne S152	Nov 2000	35°W	5°S-9°N	full
Oceanus OC365/4	Mar 2001	35°W	1°S-7°N	full
Ron Brown 0201	Feb 2002	35°W	6°N-7°N	full
Meteor M53/2	May 2002	35°W	5.5°S-8°N	full
Sonne S171	May 2003	35°W	5.5°S-6.5 °N	full
Meteor M62/2	Aug 2004	35°W	5.5°S-5°N	full
Meteor M68/2	Jun 2006	35°W	5°S-5°N	full

*Depths marked as 'full' span the entire water column.
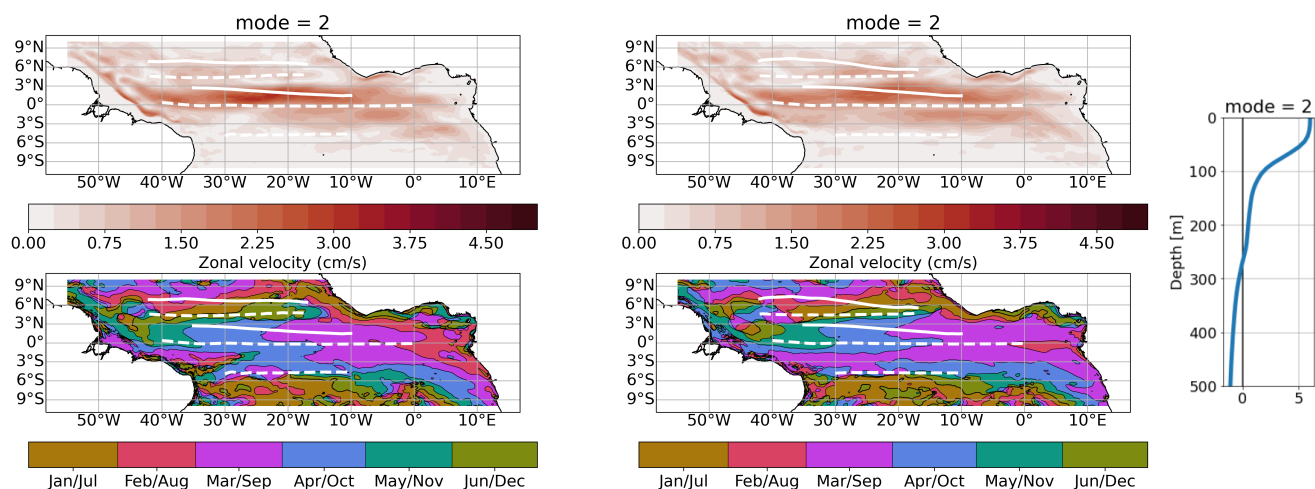
Figure A1. Amplitude (upper) and phase (lower) of second baroclinic mode, semi-annual cycle of zonal veloticy from JRA (left, 2000-2018) and CORE (right, 1991-2009) simulation. To derive the 3D zonal velocity field associated with the specific baroclinic mode, the amplitudes have to be multiplied by the corresponding vertical structure function shown on the right. The phase is given in month of the year when maximum eastward velocity occurs at the surface. Zonal white lines mark the mean latitude (Y_{CM}, Equ. 2) of the simulated surface (solid) and subsurface (dashed) currents for the respective periods.
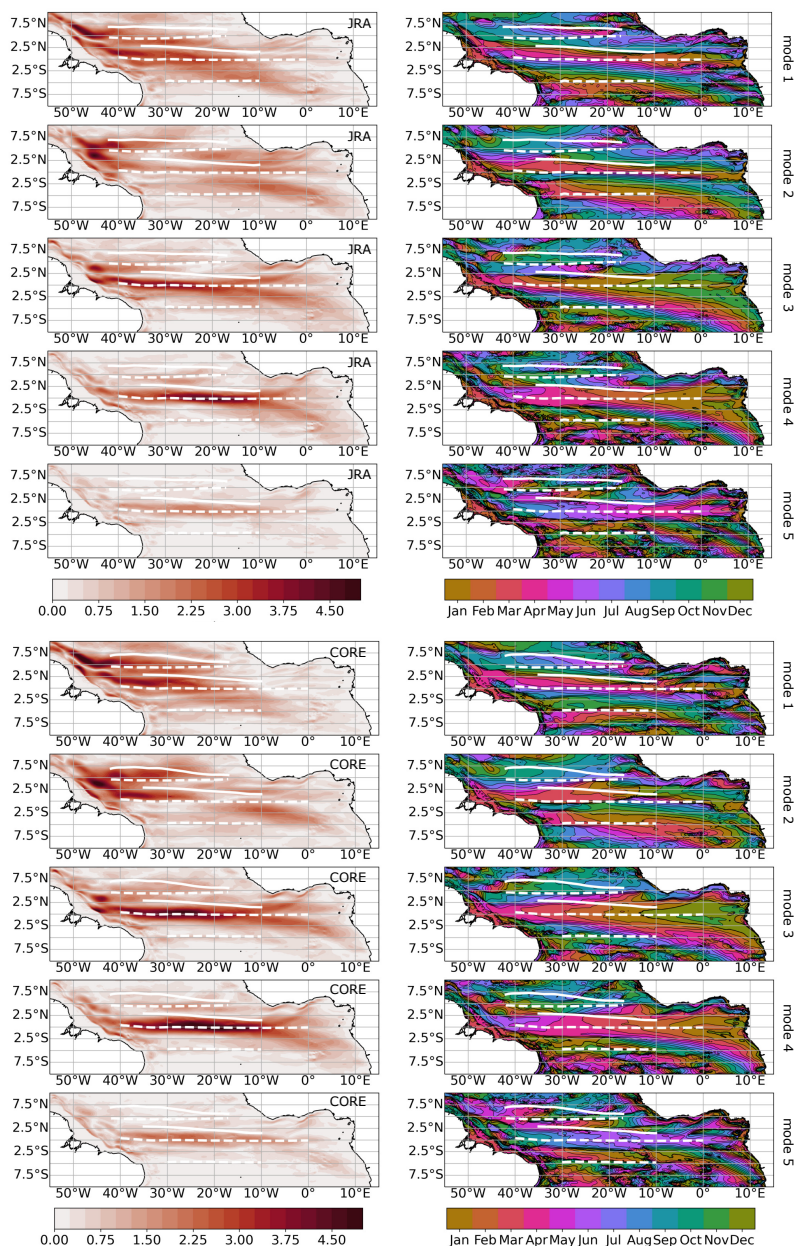
Figure A2. Amplitude (left) and phase (right) of first five baroclinic modes, annual cycle of zonal veloticy from JRA and CORE (1980-2009) simulation. To derive the 3D zonal velocity field associated with the specific baroclinic mode, the amplitudes have to be multiplied by the corresponding vertical structure function. The phase is given in month of the year when maximum eastward velocity occurs at the surface. Zonal white lines mark the mean latitude (Y_{CM}, Equ. 2) of the simulated surface (solid) and subsurface (dashed) currents for the respective periods.
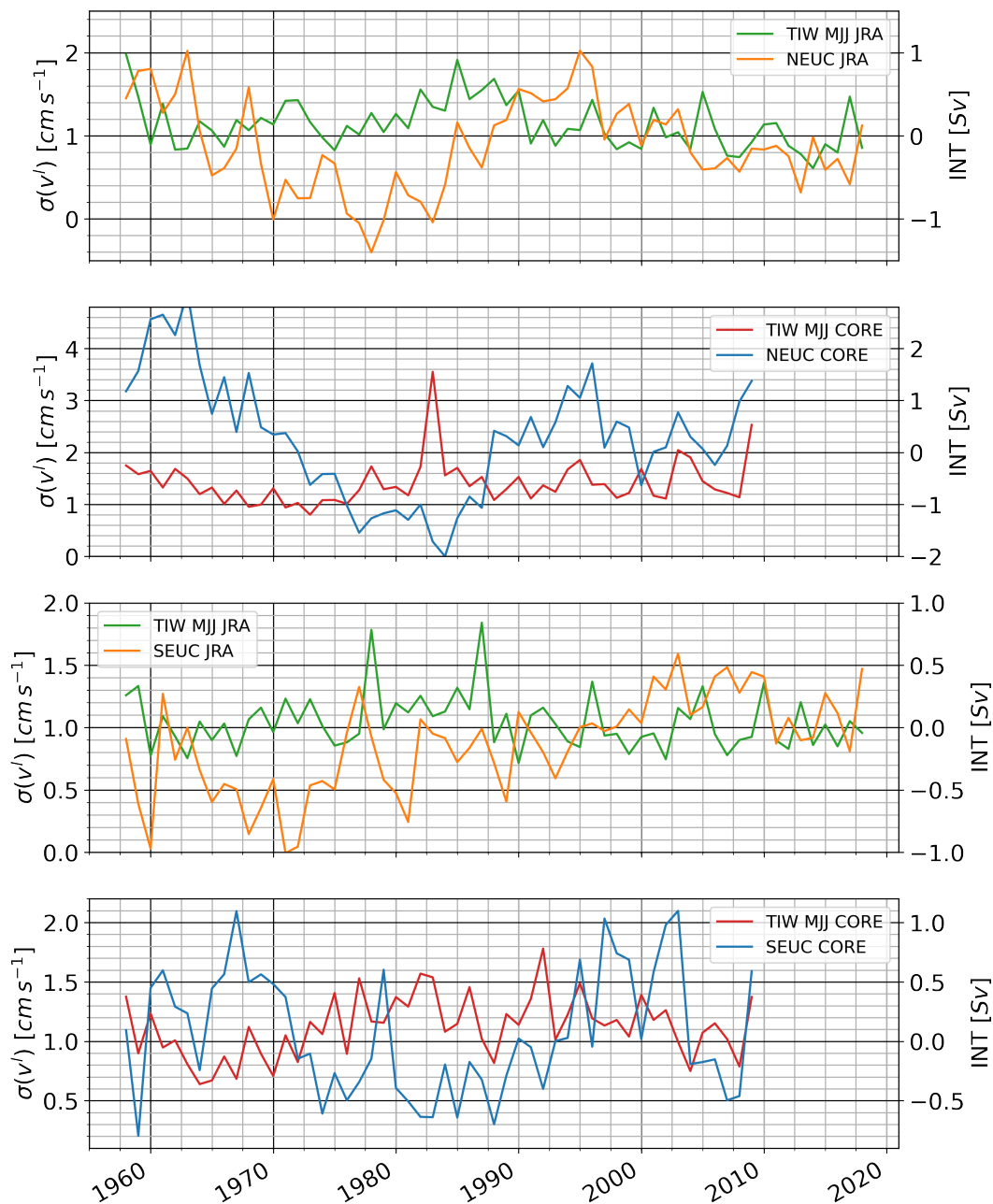
Figure A3. Long term TIW activity shown as May-June averages of monthly standard deviation of band-pass filtered meridional velocity at 160m depth in JRA_{sim} (green lines) and $CORE_{sim}$ (red lines) spatially averaged within the NEUC (top two panels) and SEUC region (bottom two panels). Also shown are the zonally averaged annual mean transport anomalies of the NEUC and SEUC in JRA_{sim} (orange lines) and $CORE_{sim}$ (blue lines).
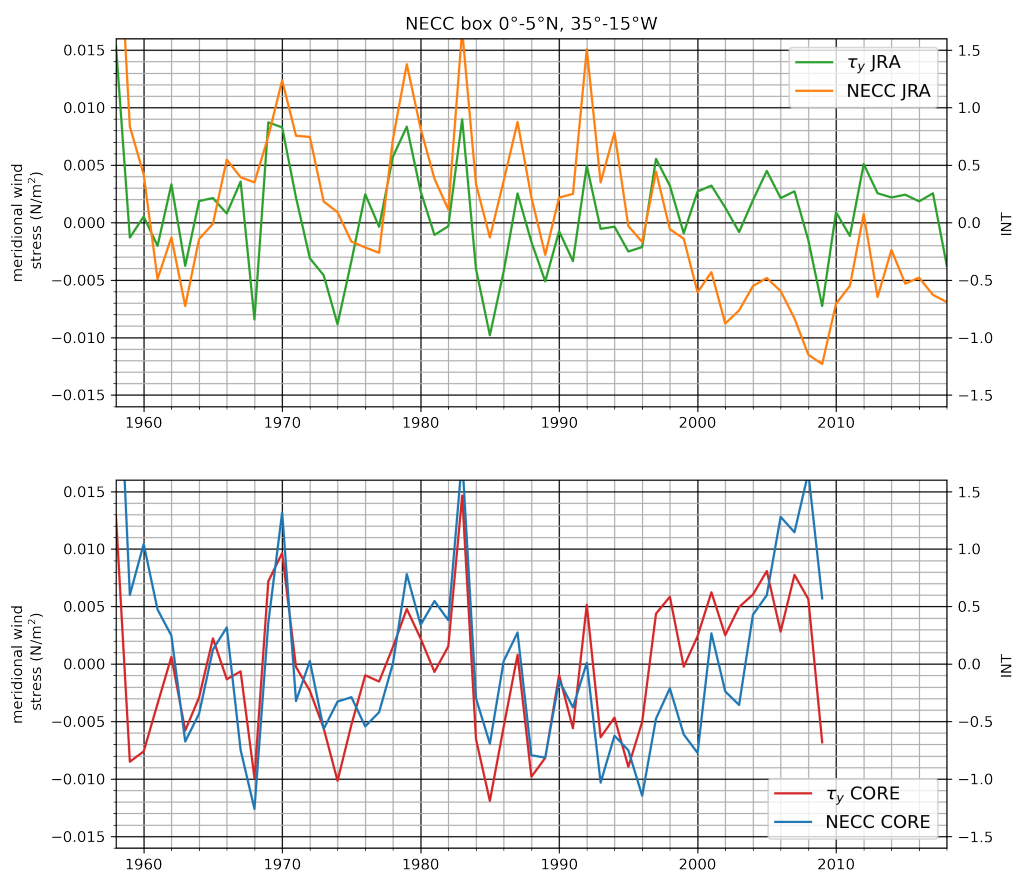
Figure A4. Annual mean meridional wind stress anomalies averages between $0°$ and $5°N$, $35°W$ and $15°W$ (green and red lines) and zonally averaged annual mean NECC transport anomalies (orange and blue lines) for JRA_{sim} (top) and $CORE_{sim}$ (bottom).
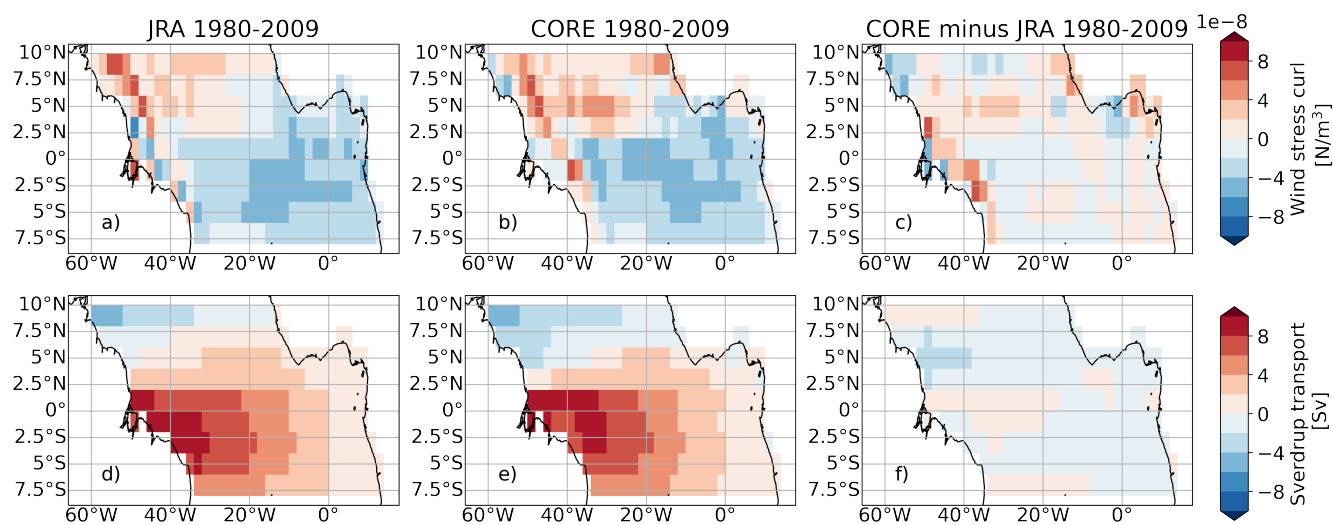
Figure A5. 1980 to 2009 mean maps of wind stress curl and Sverdrup transport calculated from wind stress data averaged in $2° \times 2°$ bins.

Author contributions. KB planned and performed the analysis, produced all figures and authored the manuscript from the first draft to the final version. FUS run the model simulations and advised in using the model output. WR provided the initial code to perform the modal decomposition of the model output. All co-authors contributed to the scientific improvement of the paper.

Competing interests. The contact author has declared that none of the authors has any competing interests.

References

Arhan, M., Treguier, A. M., Bourlès, B., and Michel, S.: Diagnosing the Annual Cycle of the Equatorial Undercurrent in the Atlantic Ocean from a General Circulation Model, Journal of Physical Oceanography, 36, 1502–1522, https://doi.org/10.1175/JPO2929.1, 2006.

Ascani, F., Wang, D., and Firing, E.: Equatorial deep jets in a simple ocean generation circulation model, pp. 87, Abstract OS33C–05 (Ocean Sciences Meeting Supp, 2006.

Assene, F., Morel, Y., Delpech, A., Aguedjou, M., Jouanno, J., Cravatte, S., Marin, F., Ménesguen, C., Chaigneau, A., Dadou, I., Alory, G., Holmes, R., Bourlès, B., and Koch-Larrouy, A.: From mixing to the large scale circulation: how the inverse cascade is involved in the formation of the subsurface currents in the gulf of guinea, Fluids, 5, 1–34, https://doi.org/10.3390/fluids5030147, 2020.

Barnier, B., Madec, G., Penduff, T., Molines, J.-M., Treguier, A.-M., Sommer, J. L., Beckmann, A., Biastoch, A., Böning, C., Dengg, J., Derval, C., Durand, E., Gulev, S., Remy, E., Talandier, C., Theetten, S., Maltrud, M., McClean, J., and Cuevas, B. D.: Impact of partial steps and momentum advection schemes in a global ocean circulation model at eddy-permitting resolution, Ocean Dynamics, 56, 543–567, https://doi.org/10.1007/s10236-006-0082-1, 2006.

Behrens, E., Våge, K., Harden, B., Biastoch, A., and Böning, C. W.: Composition and variability of the Denmark Strait Overflow Water in a high-resolution numerical model hindcast simulation, Journal of Geophysical Research: Oceans, 122, 2830–2846, https://doi.org/10.1002/2016JC012158, 2017.

Bourlès, B., Gouriou, Y., and Chuchla, R.: On the circulation in the upper layer of the western equatorial Atlantic, Journal of Geophysical Research: Oceans, 104, 21 151–21 170, https://doi.org/10.1029/1999JC900058, 1999.

Bourlès, B., D'Orgeville, M., Eldin, G., Gouriou, Y., Chuchla, R., DuPenhoat, Y., and Arnault, S.: On the evolution of the thermocline and subthermocline eastward currents in the Equatorial Atlantic, Geophysical Research Letters, 29, 32–1–32–4, https://doi.org/10.1029/2002GL015098, 2002.

Brandt, P., Schott, F. A., Provost, C., Kartavtseff, A., Hormann, V., Bourlès, B., and Fischer, J.: Circulation in the central equatorial Atlantic: Mean and intraseasonal to seasonal variability, Geophysical Research Letters, 33, 1–4, https://doi.org/10.1029/2005GL025498, 2006.

Brandt, P., Funk, A., Tantet, A., Johns, W. E., and Fischer, J.: The Equatorial Undercurrent in the central Atlantic and its relation to tropical Atlantic variability, Climate Dynamics, 43, 2985–2997, https://doi.org/10.1007/s00382-014-2061-4, good summary of SST events 2009 on page 12-13

Paper in general:
variability of different EUC characteristics such as
EUC transport,
EUC core depth ,
EUC maximum core velocity ,
and EUC core latitude .

Intro:
- EUC among strogest currents of tropical ocean.
- Weakining (strengthening) of EUC during warm (cold) events in Atlantic.
- Equatorial deep jets (EDJs) ocsillating at a period of 4.5 years. EDJs downward phase/ upward energy propagation: able to modulate subsurface/surface equ. zonal vel and hence SST.

Method:
Hilbert EOFs and regression and optimal width method

Results:
- absolute extremes EUC transport: minimum Feb 09 / maximum Oct10
- anomalous southward (northward) displacement in 2005 (2009/2010) evtl. linked to EDJs (4.5 years cycle)?
- strongest EUC transport variability during early boreal summer = onset of ECT, 2014.

Brandt, P., Bange, H. W., Banyte, D., Dengler, M., Didwischus, S.-H., Fischer, T., Greatbatch, R. J., Hahn, J., Kanzow, T., Karstensen, J., Körtzinger, A., Krahmann, G., Schmidtko, S., Stramma, L., Tanhua, T., and Visbeck, M.: On the role of circulation and mixing in the ventilation of oxygen minimum zones with a focus on the eastern tropical North Atlantic, Biogeosciences, 12, 489–512, https://doi.org/10.5194/bg-12-489-2015, 2015.

Brandt, P., Claus, M., Greatbatch, R. J., Kopte, R., Toole, J. M., Johns, W. E., and Böning, C. W.: Annual and Semiannual Cycle of Equatorial Atlantic Circulation Associated with Basin-Mode Resonance, Journal of Physical Oceanography, 46, 3011–3029, https://doi.org/10.1175/JPO-D-15-0248.1, 2016.

Brandt, P., Hahn, J., Schmidtko, S., Tuchen, F. P., Kopte, R., Kiko, R., Bourlès, B., Czeschel, R., and Dengler, M.: Atlantic Equatorial Undercurrent intensification counteracts warming-induced deoxygenation, Nature Geoscience, 14, 278–282, https://doi.org/10.1038/s41561-021-00716-1, 2021.

Burmeister, K., Lübbecke, J. F., Brandt, P., and Duteil, O.: Interannual Variability of the Atlantic North Equatorial Undercurrent and Its Impact on Oxygen, Journal of Geophysical Research: Oceans, 124, 2348–2373, https://doi.org/10.1029/2018JC014760, 2019.

Burmeister, K., Luebbecke, J. F., Brandt, P., Claus, M., and Hahn, J.: Fluctuations of the Atlantic North Equatorial Undercurrent and Associated Changes in Oxygen Transports, Geophysical Research Letters, 47, https://doi.org/10.1029/2020GL088350, 2020.

Böning, C. W., Behrens, E., Biastoch, A., Getzlaff, K., and Bamber, J. L.: Emerging impact of Greenland meltwater on deepwater formation in the North Atlantic Ocean, Nature Geoscience, 9, 523–527, https://doi.org/10.1038/ngeo2740, 2016.

Cane, M. A. and Moore, D. W.: A Note on Low-Frequency Equatorial Basin Modes, Journal of Physical Oceanography, 11, 1578–1584, https://doi.org/10.1175/1520-0485(1981)011<1578:ANOLFE>2.0.CO;2, 1981.

Carton, J. A., Cao, X., Giese, B. S., and Silva, A. M. D.: Decadal and Interannual SST Variability in the Tropical Atlantic Ocean, Journal of Physical Oceanography, 26, 1165–1175, https://doi.org/10.1175/1520-0485(1996)026<1165:DAISVI>2.0.CO;2, 1996.

Chang, P., Ji, L., and Li, H.: A decadal climate variation in the tropical Atlantic Ocean from thermodynamic air-sea interactions, Nature, 385, 516–518, https://doi.org/10.1038/385516a0, 1997.

Claus, M., Greatbatch, R. J., Brandt, P., and Toole, J. M.: Forcing of the Atlantic equatorial deep jets derived from observations, Journal of Physical Oceanography, 46, 3549–3562, https://doi.org/10.1175/JPO-D-16-0140.1, 2016.

Debreu, L., Vouland, C., and Blayo, E.: AGRIF: Adaptive grid refinement in Fortran, Computers & Geosciences, 34, 8–13, https://doi.org/10.1016/j.cageo.2007.01.009, 2008.

Delworth, T. L. and Greatbatch, R. J.: Multidecadal Thermohaline Circulation Variability Driven by Atmospheric Surface Flux Forcing, Journal of Climate, 13, 1481–1495, https://doi.org/10.1175/1520-0442(2000)013<1481:MTCVDB>2.0.CO;2, 2000.

Ding, H., Keenlyside, N. S., and Latif, M.: Seasonal cycle in the upper equatorial Atlantic Ocean, Journal of Geophysical Research, 114, C09 016, https://doi.org/10.1029/2009JC005418, 2009.

d'Orgeville, M., Hua, B. L., and Sasaki, H.: Equatorial deep jets triggered by a large vertical scale variability within the western boundary layer, Journal of Marine Research, 65, 1–25, https://doi.org/10.1357/002224007780388720, 2007.

Duteil, O., Schwarzkopf, F. U., Böning, C. W., and Oschlies, A.: Major role of the equatorial current system in setting oxygen levels in the eastern tropical Atlantic Ocean: A high-resolution model study, Geophys. Res. Lett., 41, 2033–2040, https://doi.org/10.1002/2013GL058888, 2014.

Fichefet, T. and Maqueda, M. A. M.: Sensitivity of a global sea ice model to the treatment of ice thermodynamics and dynamics, Journal of Geophysical Research: Oceans, 102, 12 609–12 646, https://doi.org/10.1029/97JC00480, 1997.

Fiorino, M.: The impact of the satellite observing system on low-fre- quency temperature variability in the ECMWF and NCEP reanalyses, p. 65–68, 2000.

Fischer, J., Brandt, P., Dengler, M., Müller, M., and Symonds, D.: Surveying the upper ocean with the ocean surveyor: A new phased array Doppler current profiler, Journal of Atmospheric and Oceanic Technology, 20, 742–751, https://doi.org/10.1175/1520-0426(2003)20<742:STUOWT>2.0.CO;2, 2003.

Fischer, J., Hormann, V., Brandt, P., Schott, F. A., Rabe, B., and Funk, A.: South Equatorial Undercurrent in the western to central tropical
705   Atlantic, Geophysical Research Letters, 35, 1–5, https://doi.org/10.1029/2008GL035753, 2008.

Frajka-Williams, E., Beaulieu, C., and Duchez, A.: Emerging negative Atlantic Multidecadal Oscillation index in spite of warm subtropics,
        Scientific Reports, 7, https://doi.org/10.1038/s41598-017-11046-x, 2017.

Fratantoni, D. M., Johns, W. E., Townsend, T. L., and Hurlburt, H. E.: Low-Latitude Circulation and Mass Transport Pathways
        in a Model of the Tropical Atlantic Ocean*, Journal of Physical Oceanography, 30, 1944–1966, https://doi.org/10.1175/1520-
710   0485(2000)030<1944:LLCAMT>2.0.CO;2, 2000.

Furue, R., McCreary, J. P., Yu, Z., and Wang, D.: Dynamics of the Southern Tsuchiya Jet*, J. Phys. Oceanogr., 37, 531–553,
        https://doi.org/10.1175/JPO3024.1, 2007.

Furue, R., Jr., J. P. M., and Yu, Z.: Dynamics of the Northern Tsuchiya Jet*, Journal of Physical Oceanography, 39, 2024–2051,
        https://doi.org/10.1175/2009JPO4065.1, 2009.

715 Goes, M., Goni, G., Hormann, V., and Perez, R. C.: Variability of the Atlantic off-equatorial eastward currents during 1993-2010 using a
        synthetic method, Journal of Geophysical Research: Oceans, 118, 3026–3045, https://doi.org/10.1002/jgrc.20186, 2013.

Greatbatch, R. J., Brandt, P., Claus, M., Didwischus, S.-H., and Fu, Y.: On the Width of the Equatorial Deep Jets, Journal of Physical
        Oceanography, 42, 1729–1740, https://doi.org/10.1175/JPO-D-11-0238.1, 2012.

Griffies, S. M., Biastoch, A., Böning, C., Bryan, F., Danabasoglu, G., Chassignet, E. P., England, M. H., Gerdes, R., Haak, H., Hallberg,
720   R. W., Hazeleger, W., Jungclaus, J., Large, W. G., Madec, G., Pirani, A., Samuels, B. L., Scheinert, M., Gupta, A. S., Severijns, C. A.,
        Simmons, H. L., Treguier, A. M., Winton, M., Yeager, S., and Yin, J.: Coordinated Ocean-ice Reference Experiments (COREs), Ocean
        Modelling, 26, 1–46, https://doi.org/10.1016/j.ocemod.2008.08.007, 2009.

Hahn, J., Brandt, P., Greatbatch, R. J., Krahmann, G., and Körtzinger, A.: Oxygen variance and meridional oxygen supply in the Tropical
        North East Atlantic oxygen minimum zone, Climate Dynamics, 43, 2999–3024, https://doi.org/10.1007/s00382-014-2065-0, 2014.

725 Hahn, J., Brandt, P., Schmidtko, S., and Krahmann, G.: Decadal oxygen change in the eastern tropical North Atlantic, Ocean Science, 13,
        551–576, https://doi.org/10.5194/os-13-551-2017, 2017.

Hazeleger, W. and Drijfhout, S.: Subtropical cells and meridional overturning circulation pathways in the tropical Atlantic, Journal of Geo-
        physical Research: Oceans, 111, 1–13, https://doi.org/10.1029/2005JC002942, 2006.

He, Y. C., Drange, H., Gao, Y., and Bentsen, M.: Simulated Atlantic Meridional Overturning Circulation in the 20th century with an ocean
730   model forced by reanalysis-based atmospheric data sets, Ocean Modelling, 100, 31–48, https://doi.org/10.1016/j.ocemod.2015.12.011,
        2016.

Heukamp, F. O., Brandt, P., Dengler, M., Tuchen, F. P., McPhaden, M. J., and Moum, J. N.: Tropical Instability Waves and Wind-Forced
        Cross-Equatorial Flow in the Central Atlantic Ocean, Geophysical Research Letters, 49, https://doi.org/10.1029/2022GL099325, 2022.

Hormann, V. and Brandt, P.: Atlantic Equatorial Undercurrent and associated cold tongue variability, Journal of Geophysical Research:
735   Oceans, 112, 1–18, https://doi.org/10.1029/2006JC003931, 2007.

Hormann, V., Lumpkin, R., and Foltz, G. R.: Interannual North Equatorial Countercurrent variability and its relation to tropical Atlantic
        climate modes, Journal of Geophysical Research: Oceans, 117, n/a–n/a, https://doi.org/10.1029/2011JC007697, 2012.

Hsin, Y. C. and Qiu, B.: Seasonal fluctuations of the surface North Equatorial Countercurrent (NECC) across the Pacific basin, Journal of
        Geophysical Research: Oceans, 117, 1–17, https://doi.org/10.1029/2011JC007794, 2012.

Hua, B. L., Marin, F., and Schopp, R.: Three-Dimensional Dynamics of the Subsurface Countercurrents and Equatorial Thermostad. Part II: Influence of the Large-Scale Ventilation and of Equatorial Winds, Journal of Physical Oceanography, 33, 2588–2609, https://doi.org/10.1175/1520-0485(2003)033<2610:TDOTSC>2.0.CO;2, 2003.

Hurrell, J. W. and Trenberth, K. E.: Difficulties in obtaining reliable temperature trends: reconciling the surface and satellite microwave sounding unit records, Journal of Climate, 11, 945–967, https://doi.org/10.1175/1520-0442(1998)011<0945:DIORTT>2.0.CO;2, 1998.

Hüttl-Kabus, S. and Böning, C. W.: Pathways and variability of the off-equatorial undercurrents in the Atlantic Ocean, Journal of Geophysical Research: Oceans, 113, 1–14, https://doi.org/10.1029/2007JC004700, 2008.

Ishida, A., Mitsudera, H., Kashino, Y., and Kadokura, T.: Equatorial Pacific subsurface countercurrents in a high-resolution global ocean circulation model, Journal of Geophysical Research C: Oceans, 110, 1–21, https://doi.org/10.1029/2003JC002210, 2005.

Jochum, M. and Malanotte-Rizzoli, P.: A New Theory for the Generation of the Equatorial Subsurface Countercurrents, Journal of Physical Oceanography, 34, 755–771, https://doi.org/10.1175/1520-0485(2004)034<0755:ANTFTG>2.0.CO;2, 2004.

Johns, W. E., Zantopp, R. J., and Goni, G.: Cross-gyre transport by North Brazil Current rings, https://doi.org/10.1016/S0422-9894(03)80156-3, 2003.

Johnson, G. C. and Moore, D. W.: The Pacific Subsurface Countercurrents and an Inertial Model*, Journal of Physical Oceanography, 27, 2448–2459, https://doi.org/10.1175/1520-0485(1997)027<2448:TPSCAA>2.0.CO;2, 1997.

Kessler, W. S., Johnson, G. C., and Moore, D. W.: Sverdrup and nonlinear dynamics of the Pacific equatorial currents, Journal of Physical Oceanography, 33, 994–1008, https://doi.org/10.1175/1520-0485(2003)033<0994:SANDOT>2.0.CO;2, 2003.

Kobayashi, C. and Iwasaki, T.: Brewer-Dobson circulation diagnosed from JRA-55, Journal of Geophysical Research: Atmospheres, 121, 1493–1510, https://doi.org/10.1002/2015JD023476, 2016.

Kopte, R., Brandt, P., Claus, M., Greatbatch, R. J., and Dengler, M.: Role of Equatorial Basin-Mode Resonance for the Seasonal Variability of the Angola Current at 11S, Journal of Physical Oceanography, 48, 261–281, https://doi.org/10.1175/JPO-D-17-0111.1, 2018.

Lee, T., Lagerloef, G., Kao, H. Y., McPhaden, M. J., Willis, J., and Gierach, M. M.: The influence of salinity on tropical Atlantic instability waves, Journal of Geophysical Research: Oceans, 119, 8375–8394, https://doi.org/10.1002/2014JC010100, 2014.

Levitus, S., Boyer, T. P., Conkright, M. E., Brien, T. O., Antonov, J., Stephens, C., Stathoplos, L., Johnson, D., and Gelfeld, R.: NOAA Atlas NESDIS 18,World Ocean Database 1998: Volume 1: Introduction, 1998.

Marin, F., Hua, B. L., and Wacongne, S.: The equatorial thermostad and subsurface countercurrents in the light of the dynamics of atmospheric Hadley cells, Journal of Marine Research, 58, 405–437, https://doi.org/10.1357/002224000321511098, 2000.

Marin, F., Schopp, R., and Hua, B. L.: Three-dimensional dynamics of the subsurface countercurrents and equatorial thermostad. Part II: Influence of the large-scale ventilation and of equatorial winds, Journal of Physical Oceanography, 33, 2610–2626, https://doi.org/10.1175/1520-0485(2003)033<2610:TDOTSC>2.0.CO;2, 2003.

McCreary, J. P. and Lu, P.: Interaction between the subtropical and equatorial ocean circulations: The subtropical cell, Journal of Physical Oceanography, 24, 466–497, https://doi.org/doi:10.1175/1520-0485(1994)024<0466:IBTSAE>2.0.CO;2, 1994.

McCreary, J. P., Lu, P., and Yu, Z.: Dynamics of the Pacific Subsurface Countercurrents, Journal of Physical Oceanography, 32, 2379–2404, https://doi.org/10.1175/1520-0485(2002)032<2379:DOTPSC>2.0.CO;2, 2002.

McPhaden, M. J.: On the Dynamics of Equatorial Subsurface Countercurrents, Journal of Physical Oceanography, 14, 1216–1225, https://doi.org/10.1175/1520-0485(1984)014<1216:OTDOES>2.0.CO;2, 1984.

Molinari, R. L., Bauer, S., Snowden, D., Johnson, G. C., Bourles, B., Gouriou, Y., and Mercier, H.: A comparison of kinematic evidence for tropical cells in the Atlantic and Pacific oceans, Elsevier Oceanography Series, 68, 269–286, https://doi.org/10.1016/S0422-9894(03)80150-2, 2003.

Olivier, L., Reverdin, G., Hasson, A., and Boutin, J.: Tropical Instability Waves in the Atlantic Ocean: Investigating the Relative Role of Sea Surface Salinity and Temperature From 2010 to 2018, Journal of Geophysical Research: Oceans, 125, https://doi.org/10.1029/2020JC016641, 2020.

Perez, R. C., Lumpkin, R., Johns, W. E., Foltz, G. R., and Hormann, V.: Interannual variations of Atlantic tropical instability waves, Journal of Geophysical Research: Oceans, 117, 1–13, https://doi.org/10.1029/2011JC007584, 2012.

Perez, R. C., Hormann, V., Lumpkin, R., Brandt, P., Johns, W. E., Hernandez, F., Schmid, C., and Bourlès, B.: Mean meridional currents in the central and eastern equatorial Atlantic, Climate Dynamics, 43, 2943–2962, https://doi.org/10.1007/s00382-013-1968-5, in this study, measurements collected primarily along
23°W and 10°W during the past two decades are used for the first time to describe: (1) the long-term mean cross- equatorial and vertical structure of the meridional currents in the central and eastern equatorial Atlantic, and (2) the seasonal means during the months December to May (hereafter Dec–May) when the Atlantic cold tongue is absent or weak and June to November (hereafter Jun–Nov) when the cold tongue is most pronounced and meridional velocity may play a role in the development of non- canonical Atlantic Nin
˷o events.

Introduction:
- shallow overturning circulation cells (tropical cells, TCs) dominate meridional currents along 23°W an 10°W
- TCs appear as near surface, near equ. maxima of much larger subropical cells
– TCs confined to upper 100m, characterized by wind-driven equ. upwelling, poliward wind driven flow in ther surface limb, off-equ. downwelling at about +/- 3-5° latitude, equatorward geostrophic flow in subsurface limb
- strong fronts boundig seasonal equu. Atlantic Cold tongue exhibit large undulations due to TIW and lead to complexity of TCs
- TIW and CT most pronounced in boreal summer associated with increased southeasterly trade winds and enhancement of the shear berween the equatorial zonal currents
- 2009: equatorial flow (30-100m) changes direction after onset of CT
- equatorial Atlantic circulation from surface to thermocline dominated by TIWs and mesoscale phenomena
- meridional currents play important role in AMM by advecting wind-driven warm temperature anomalies induced immediately north of the equ. towards the equatorial region (richter)

Data: Shipbaord data, Drifter, Argo, OSCAR, Moored current measurements, Reanalysis product

Results:
- northern TC shallower than southern one
- northern TC extend into the southern Hemnisphere over equator
- southern fow in subsurface limb in both TCs (likely due to smal number of samples)
- transpor in southern TC larger than in nothern one
- variabilty associated with position of northern cell larger than southern one
-TC asymmetry due to wind asymmetry (ITCZ)
- maximum equatorward flow druingb. summer when CT is most pronounced
- in OSCAR simulation advection of cold SST anomalies into cold tongue, but no observational evidence!, 2014.

Peterson, R. G. and Stramma, L.: Upper-level circulation in the South Atlantic Ocean, Progress in Oceanography, 26, 1–73, https://doi.org/10.1016/0079-6611(91)90006-8, 1991.

Rabe, B., Schott, F. A., and Köhl, A.: Mean Circulation and Variability of the Tropical Atlantic during 1952–2001 in the GECCO Assimilation Fields, Journal of Physical Oceanography, 38, 177–192, https://doi.org/10.1175/2007JPO3541.1, 2008.

Rosell-Fieschi, M., Pelegrí, J. L., and Gourrion, J.: Zonal jets in the equatorial Atlantic Ocean, Progress in Oceanography, 130, 1–18, https://doi.org/10.1016/j.pocean.2014.08.008, 2015.

Schott, F. A., Fischer, J., and Stramma, L.: Transports and Pathways of the Upper-Layer Circulation in the Western Tropical Atlantic, Journal of Physical Oceanography, 28, 1904–1928, https://doi.org/10.1175/1520-0485(1998)028<1904:TAPOTU>2.0.CO;2, 1998.

Schott, F. A., Jr., J. P. M., and Johnson, G. C.: Shallow Overturning Circulations of the Tropical-Subtropical Oceans, Earth's Climate, 147, 261–304, 2004.

815 Schubert, R., Schwarzkopf, F. U., Baschek, B., and Biastoch, A.: Submesoscale Impacts on Mesoscale Agulhas Dynamics, Journal of Advances in Modeling Earth Systems, 11, 2745–2767, https://doi.org/10.1029/2019MS001724, 2019.

Schwarzkopf, F. U., Biastoch, A., Böning, C. W., Chanut, J., Durgadoo, J. V., Getzlaff, K., Harlaß, J., Rieck, J. K., Roth, C., Scheinert, M. M., and Schubert, R.: The INALT family – a set of high-resolution nests for the Agulhas Current system within global NEMO ocean/sea-ice configurations, Geoscientific Model Development, 12, 3329–3355, https://doi.org/10.5194/gmd-12-3329-2019, 2019.

820 Steele, M., Morley, R., and Ermold, W.: PHC: A Global Ocean Hydrography with a High-Quality Arctic Ocean, Journal of Climate, 14, 2079–2087, https://doi.org/10.1175/1520-0442(2001)014<2079:PAGOHW>2.0.CO;2, 2001.

Stewart, K. D., Hogg, A. M. C., Griffies, S. M., Heerdegen, A. P., Ward, M. L., Spence, P., and England, M. H.: Vertical resolution of baroclinic modes in global ocean models, Ocean Modelling, 113, 50–65, https://doi.org/10.1016/J.OCEMOD.2017.03.012, 2017.

Stramma, L., Hüttl, S., and Schafstall, J.: Water masses and currents in the upper tropical northeast Atlantic off northwest Africa, Journal of
825 Geophysical Research: Oceans, 110, 1–18, https://doi.org/10.1029/2005JC002939, 2005.

Stramma, L., Brandt, P., Schafstall, J., Schott, F., Fischer, J., and Körtzinger, A.: Oxygen minimum zone in the North Atlantic south and east of the Cape Verde Islands, Journal of Geophysical Research: Oceans, 113, 1–15, https://doi.org/10.1029/2007JC004369, 2008.

Sverdrup, H. U.: Wind-Driven Currents in a Baroclinic Ocean; with Application to the Equatorial Currents of the Eastern Pacific, Proceedings of the National Academy of Sciences, 33, 318–326, https://doi.org/10.1073/pnas.33.11.318, 1947.

830 the NEMO team, G. M. .: NEMO ocean engine, 2016.

Thierry, V., Treguier, A. M., and Mercier, H.: Numerical study of the annual and semi-annual fluctuations in the deep equatorial Atlantic Ocean, Ocean Modelling, 6, 1–30, https://doi.org/10.1016/S1463-5003(02)00054-9, 2004.

Tsujino, H., Urakawa, S., Nakano, H., Small, R. J., Kim, W. M., Yeager, S. G., Danabasoglu, G., Suzuki, T., Bamber, J. L., Bentsen, M., Böning, C. W., Bozec, A., Chassignet, E. P., Curchitser, E., Dias, F. B., Durack, P. J., Griffies, S. M., Harada, Y., Ilicak, M., Josey, S. A.,
835 Kobayashi, C., Kobayashi, S., Komuro, Y., Large, W. G., Sommer, J. L., Marsland, S. J., Masina, S., Scheinert, M., Tomita, H., Valdivieso, M., and Yamazaki, D.: JRA-55 based surface dataset for driving ocean–sea-ice models (JRA55-do), Ocean Modelling, 130, 79–139, https://doi.org/10.1016/j.ocemod.2018.07.002, 2018.

Tuchen, F. P., Lübbecke, J. F., Schmidtko, S., Hummels, R., and Böning, C. W.: The Atlantic Subtropical Cells inferred from observations, Journal of Geophysical Research: Oceans, p. 2019JC015396, https://doi.org/10.1029/2019JC015396, 2019.

840 Tuchen, F. P., Brandt, P., Lübbecke, J. F., and Hummels, R.: Transports and Pathways of the Tropical AMOC Return Flow From Argo Data and Shipboard Velocity Measurements, Journal of Geophysical Research: Oceans, 127, https://doi.org/10.1029/2021JC018115, 2022a.

Tuchen, F. P., Perez, R. C., Foltz, G. R., Brandt, P., and Lumpkin, R.: Multidecadal Intensification of Atlantic Tropical Instability Waves, Geophysical Research Letters, https://doi.org/10.1029/2022gl101073, 2022b.

Urbano, D. F., Jochum, M., and da Silveira, I. C.: Rediscovering the second core of the Atlantic NECC, Ocean Modelling, 12, 1–15,
845 https://doi.org/10.1016/j.ocemod.2005.04.003, 2006.

Urbano, D. F., Almeida, R. A. D., and Nobre, P.: Equatorial undercurrent and North equatorial countercurrent at 38W: A new perspective from direct velocity data, Journal of Geophysical Research: Oceans, 113, 1–16, https://doi.org/10.1029/2007JC004215, 2008.

Wacongne, S.: Dynamical regimes of a fully nonlinear stratified model of the Atlantic equatorial undercurrent, Journal of Geophysical Research, 94, 4801, https://doi.org/10.1029/JC094iC04p04801, 1989.

850 Wang, C.: Subthermocline tropical cells and equatorial subsurface countercurrents, Deep-Sea Research Part I: Oceanographic Research
        Papers, 52, 123–135, https://doi.org/10.1016/j.dsr.2004.08.009, 2005.

    Xie, S. and Carton, J.: Tropical Atlantic variability: Patterns, mechanisms, and impacts, Geophysical Monograph Series, 147, 121–142,
        https://doi.org/10.1029/147GM07, 2004.